

HYDROGEN EMBRITTLEMENT PROCESSES IN MICROALLOYED STEEL NOTCHED TENSILE SAMPLES

A. Cayón¹, F. Gutiérrez-Solana¹, B. Arroyo^{1,*}, J.A. Álvarez¹

¹LADICIM, Depto. de Ing. del Terreno y de los Materiales, University of Cantabria
Avda. de los Castros, 44, 39005 Santander, Cantabria, Spain

*arroyob@unican.es

Abstract

In this work, two microalloyed steels, one used for oil&gas pipelines and the other one for structural components in hydrotreating reactors in petrochemical industries, have been studied under hydrogen embrittlement (HE) conditions. They have been cathodically charged with hydrogen under different aggressive conditions, its hydrogen content being determined afterwards. In order to know the effect of triaxiality on the HE behaviour of this steel, two different types of axisymmetric round notched tensile specimens have been tested under continuous hydrogen charging processes, whilst varying cathodic charging conditions and loading rate. The effects on the global mechanical characterization have been analysed, as well as the correlation between the observed fracture micromechanisms with both local environmental (as hydrogen concentration) and mechanical conditions (as hydrostatic stress and plastic strain determined with a finite elements analysis). Also, subcritical cracking due to embrittlement has been analysed and compared with those obtained by fracture mechanics standardised specimens.

Keywords: Hydrogen Embrittlement, Notched Samples, Hydrostatic Stress, Displacement Rate, Fracture Toughness, FAD diagram.

1. Introduction

The exponential increase of the petroleum derivatives consumption during the last decades is the origin of the current progressive decrease of the accessible oil reserves. It has been then necessary to find new petroleum sources farther from the coast, and at much greater depths and/or more severe working conditions [1], thus increasing the oil&gas transportation pipeline systems requirements, too. Therefore, metallic alloys, mainly new generation microalloyed steels, have been developed to support new applications for pipeline systems and structural components, optimising: the mechanical strength to improve transportation conditions at high pressures, the toughness to avoid problems with brittle fracture at low temperature and under aggressive environmental conditions, the operability to obtain good welds, the economic cost, and finally the resistance to environmental damage, as for example Hydrogen Embrittlement (HE) processes, very common in the previous applications.

The role of hydrogen in metallic materials [2] [3] [4] has been known for a long time. Hydrogen absorption into steel is mainly produced in two ways. The first possible way is

assisted by electrochemical processes such as cathodic polarisation [5], which is massively employed as protection against corrosion in offshore elements and submarine pipelines. The second way is the direct exposition of the metal to hydrogen in gaseous state [6], as it occurs in high pressure and temperature hydrotreating reactors, or in oil&gas pipelines at high pressures and permanent contact to H₂S.

Once hydrogen has been absorbed inside the metal, it is transported, or diffused, through the microstructure preferably to the most solicited areas, being trapped in certain local areas, the hydrogen traps [7] [8], which, as well as reducing diffusivity, can be positive or negative to enhance material embrittlement. The variables that govern the diffusion process are then the microstructure and the chemical composition [9], that define matrix diffusivity as well as trapping issues associated to the heterogeneities present in the metallic matrix as inclusions, precipitates, microcracks, dislocations..., as well as the grain boundaries.

There are different theories that study local mechanisms concerning hydrogen embrittlement. Among them, the most relevant are “the pressure theory”, the “decohesion theory” and “loss of plasticity at local level”, all of them collected in [10]. All these theories have in common the fact that, from a mechanical point of view, the critical zones for HIC processes are those where maximal triaxial stress states are developed, since there the volumetric strain is maximum. This fact (high volumetric strain) favours hydrogen accumulation, in addition to contributing to the cracks propagation for being the most unfavourable stress state (triaxiality).

There are numerous researches related to the mechanical properties loss due to hydrogen presence in metals [11] [12] [13] [14], as well as many other linked to hydrogen diffusion and accumulation processes [15] [16] [17] [18] [19]. Also, there are some works that explain the influence at a local level of the material intrinsic variables, as microstructure, or stresses and strain states present in that zone, under which there are suitable circumstances for the appearance of the HIC phenomenon [20] [21]. Finally, less common are the scientific publications about modeling the phenomenon of embrittlement at a local level, which leads to the start of HIC [22] [23].

This paper analyses, for different geometries, the main affected area to initiate embrittlement mechanisms, that leads to HIC and embrittlement of the components as a function of microstructure, stress and strain distribution and hydrogen concentration.

2. Materials and environments employed for hydrogen charging

2.1. Materials selected

Two microalloyed steels were selected, considering their different chemical composition, microstructure and, therefore, mechanical resistance. The chemical composition of both steels is presented in Table 1, together with their microstructure in Figure 1.

The first one is an X65 steel, following API denomination [24], which is mainly used for oil&gas pipelines, working at high pressures and in contact with H₂S. It has a ferritic-pearlitic microstructure, and is characterised for having a very low carbon content together with vanadium and aluminium as main microalloying elements. It was received

in a rolled 30 mm thick plate, from which tensile specimens were machined along T orientation (the strongest one) and C(T) fracture ones in TL orientation.

The second material selected is a 3Cr-1Mo-0.25V, according to [25], and is mainly employed to manufacture structural components on hydro-treating reactors operating under high temperatures and hydrogen gas pressures. This material was normalised at 950°C and quenched in water, then tempered at 675°C during 3 hours. Accordingly, it has a tempered bainitic microstructure, and has a higher carbon content compared to X65 steel, together with chromium, molybdenum and vanadium as main microalloying elements. It was received in a 70mm thick prismatic coupon, from which tensile specimens were machined along T orientation and fracture ones in TS orientation.

In both cases, tensile tests were carried out on $\phi 10$ mm cylindrical specimens according to EN 10002-1 [26] and ASTM E8 [27], and fracture tests on C(T) B=25mm thick specimens incorporating 0.1B side grooves according to ESIS P1-92 [28] and ASTM E1820 [29], finally, hardness tests HV0.3 were carried out according ASTM E384 [30] by applying loads of 300g during 20 seconds. The results of this conventional characterisation are summarised in Table 2.

Table 1. Chemical composition of the steels employed in this work.

| | C | Mn | Si | Ni | Cr | Mo | Cu | Al | Sn | S | P | Ti | V |
|----------------------|-------|-------|-------|-------|-------|-------|-------|-------|-------|-------|-------|-------|-------|
| X65 | 0.066 | 1.31 | 0.28 | 0.022 | 0.044 | 0.082 | 0.32 | 0.036 | 0.002 | 0.002 | 0.010 | 0.006 | 0.065 |
| 3Cr-1Mo-0.25V | 0.13 | 0.524 | 0.057 | 0.196 | 3.02 | 0.97 | 0.048 | - | 0.004 | 0.004 | 0.006 | - | 0.232 |

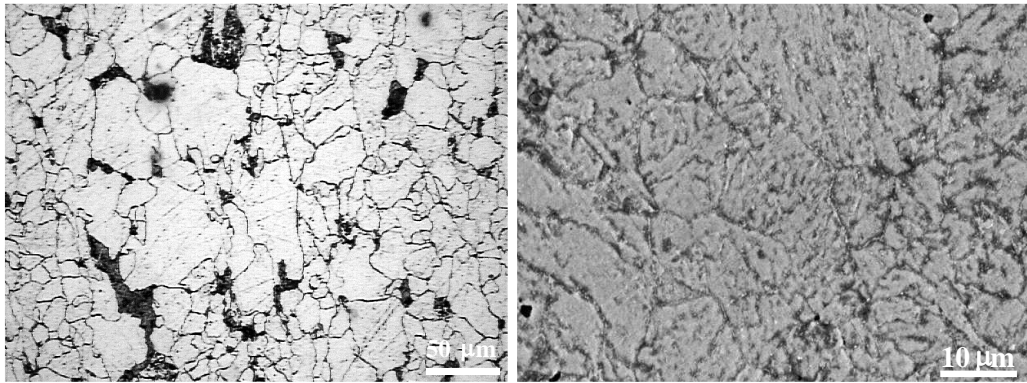


Figure 1. Microstructure of the X65 (left) and 3Cr-1Mo-0.25V (right) steels.

Table 2. Main mechanical parameters of the steels employed in this work.

| PARAMETER | | | X65 | 3Cr-1Mo-0.25V |
|-----------------------|--|----------|---|---|
| Tensile behaviour | Yield stress, S_y , (MPa) | | 467 | 642 |
| | Tensile strength, S_u , (MPa) | | 541 | 768 |
| | Young modulus, E , (GPa) | | 207.4 | 211.4 |
| | Strain at max load, ϵ_{\max} , (%) | | 14.7 | 5.8 |
| | Elongation at break, ΔL , (%) | | 24.5 | 12.3 |
| | Area reduction, AR (%) | | 73.2 | 66.4 |
| | Ramberg-Osgood | α | 12.99 | 0.354 |
| n | | 6.56 | 18.50 | |
| Fracture behaviour | $J_{0.2/BL}$ (kJ/m ²) | | 650 | 241 |
| | J (kJ/m ²) – Δa (mm) curve | | $J = 859.64 \cdot (\Delta a)^{0.30873}$ | $J = 496.38 \cdot (\Delta a)^{0.57588}$ |
| Hardness (HV 0.3) | | | 190 ± 7 | 258 ± 9 |

2.2. Environments and hydrogen contents

The focus of this work is to model the behavior of the steels previously described in response to hydrogen embrittlement processes, in order to reproduce their working operations when used in oil&gas and petrochemical facilities. To simulate this environmental harsh conditions, cathodic polarisation is used to produce hydrogen to be adsorbed and absorbed into the cylindrical small samples, in as-received state (without any deformation).

The acid electrolyte consisted of a 1N H₂SO₄ solution in distilled H₂O, containing 10mg of an As₂O₃ solution and 10 drops of CS₂ per liter of dissolution; the As₂O₃ solution was prepared following the Pressouyre's method [31]. The specimen, a platinum wire and the saturated calomel electrode were used as the working electrode, the counter electrode and the reference electrode respectively. The pH was measured in the range 0.65-0.80 during the tests and at room temperature (20±2 °C). The aqueous solution was in continuous stirring and/or circulation [32] to remove hydrogen bubbles on the specimen surface, and prevent localised corrosion deposits (e.g., pits) or local environmental conditions. A schematic of the cathodic polarisation set-up employed during the tests is shown in Figure 2.

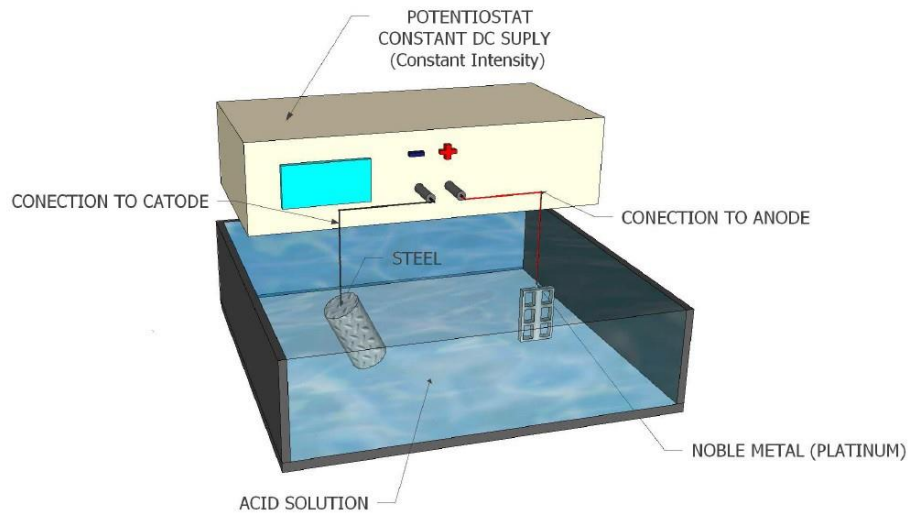


Figure 2. *Schematic of the cathodic polarization set-up employed.*

The aggressiveness of the environment was controlled by the application of three different levels of current density of 1, 5 and 10 mA/cm² of submerged sample, imposed between the steel and the platinum. In order to quantify the hydrogen absorption capacity of each one of the materials in the three mentioned situations, hydrogen content tests were carried out by the hot extraction technique, employing the simple acetone cleaning method and following the overall recommendations suggested in [33]. A total of 10 samples was tested for each scenario, adopting the mean \pm SD as a result, which are displayed in Table 3.

Table 3. *Hydrogen concentration for the different steels and conditions used.*

| | X65 | 3Cr-1Mo-0.25V |
|-----------------------------|-----------------|----------------------|
| As received (ppm) | 0.29 \pm 0.05 | 1.41 \pm 0.20 |
| 1 mA/cm ² (ppm) | 1.08 \pm 0.40 | 4.20 \pm 0.30 |
| 5 mA/cm ² (ppm) | 1.25 \pm 0.50 | 8.04 \pm 0.70 |
| 10 mA/cm ² (ppm) | 1.32 \pm 0.30 | 11.38 \pm 0.50 |

In both cases, extreme hydrogen conditions multiplies the hydrogen content in the material by over 4 and 8 respectively. Nevertheless, the absolute increase in hydrogen concentration is much more important in the 3Cr-1Mo-0.25V (10 ppm approx.), which has a bainitic microstructure with higher precipitate and dislocation density than in X65 with a ferritic-pearlitic microstructure with higher cleanliness (less precipitates and inclusions).

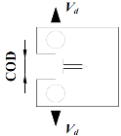
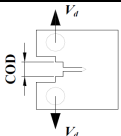
3. Background research to be considered

In a previous work, the selected materials were characterised facing HIC, in order to obtain the fracture toughness in aggressive environment, K_{I-HC} . An analytical methodology, based on the GE-EPRI-1931 procedure and the concept of iso-a curves [34]

together with the elastic and plastic components of J integral, was employed; its application is described in detail in [13] [23]. K_{I-HC} is taken as the stress intensity factor calculated at the point of the P-COD register where subcritical propagation ends and the final failure of the specimen takes place, which is calculated using the actual crack size at that point, obtained by the intersection between the corresponding iso-a curve with the test P-COD record [23].

For this purpose, B=25 mm thick C(T) pre-cracked specimens obtained according to [29] were employed, tested at very slow rates according to [32]. The environments employed were the aforementioned ones of cathodic polarisation at 1, 5 and 10 mA/cm², while the testing rates chosen were 10⁻⁷, 10⁻⁸ and 10⁻⁹ m/s, for three displacement rates that will be called V_{d1} , V_{d2} and V_{d3} . The numerical results of K_{I-HC} are presented in Table 4, while some examples of the embrittled fracture surfaces obtained in all the cases are presented in Figure 3, showing brittle mechanisms in all the cases, with the presence of decohesion, cleavage and intergranular cracking, being the presence of these features slightly higher at the lowest rate.

Table 4. Hydrogen fracture toughness in aggressive environment, K_{I-HIC} , of the steels studied in the environments described.

|  | X65 K_{I-HC} (MPa·m ^{1/2}) C(T) | | |
|---|---|-----------------------------|------------------------------|
| | I = 1 mA/cm ² | I = 5 mA/cm ² | I = 10 mA/cm ² |
| V_{d-1} rate 10 ⁻⁷ m/s | - | 81 | - |
| V_{d-2} rate 10 ⁻⁸ m/s | 59 | 48 | 52 |
| V_{d-3} rate 10 ⁻⁹ m/s | - | 46 | - |
|  | 3Cr-1Mo-0.25V K_{I-HC} (MPa·m ^{1/2}) C(T) | | |
| | I = 1 mA/cm ² | I = 5 mA/cm ² | I = 10 mA/cm ² |
| V_{d-1} rate 10 ⁻⁷ m/s | - | 93 | - |
| V_{d-2} rate 10 ⁻⁸ m/s | 105 | 67 | 47 |
| V_{d-3} rate 10 ⁻⁹ m/s | - | 62 | - |

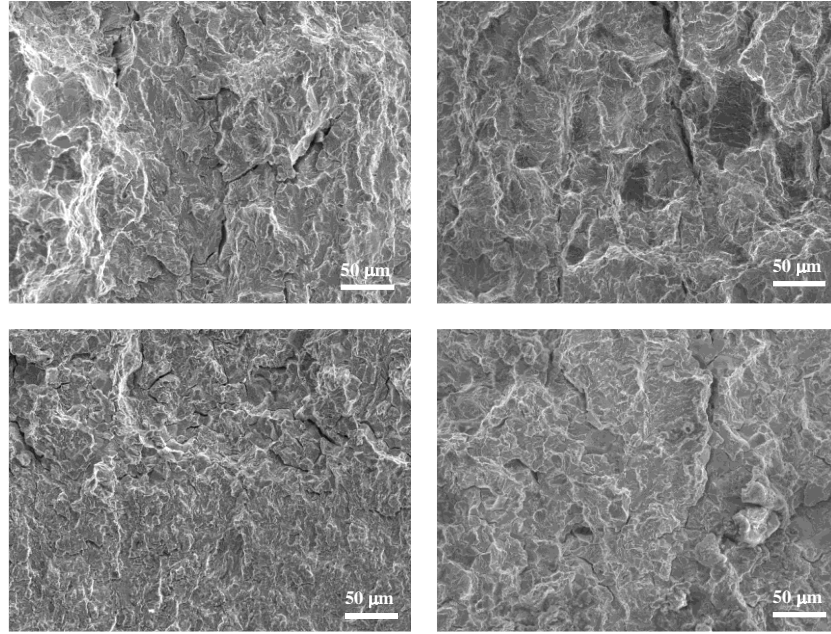


Figure 3. *Fractography from C(T) slow strain rate tests at the subcritical propagation onset; top: X65 under 5 mA/cm² at 10⁻⁷ m/s (left) and 10⁻⁹ m/s (right); bottom: 3Cr-1Mo-0.25V under 5 mA/cm² at 10⁻⁷ m/s (left) and 10⁻⁹ m/s (right).*

4. Experimental methodology

4.1. Geometries and testing rates for axisymmetric notched cylindrical SSRT

In order to analyse the geometrical effect on the influence of hydrogen presence on the mechanical behaviour of the steels under study, the experimental work has been carried out on axisymmetric round-notched tensile specimens, considering two different notch profiles. The two geometries selected based on the European Standards ESIS P6-98 [35] are shown in Figure 4. Both geometries keep the same net section at the remaining ligament, of 5 mm of diameter, varying only the machined notch radius of 5 mm or 0.5 mm; therefore, the different radius induce important variations in stress triaxiality: vital fact in hydrogen induced cracking and embrittlement phenomena [36]. Onwards, the 5 mm notch radius (and 5 mm remaining ligament) geometry is named NT 5-5, while the 0.5 mm notch radius (and 5 mm remaining ligament) is NT0.5-5, as indicated in Figure 4.

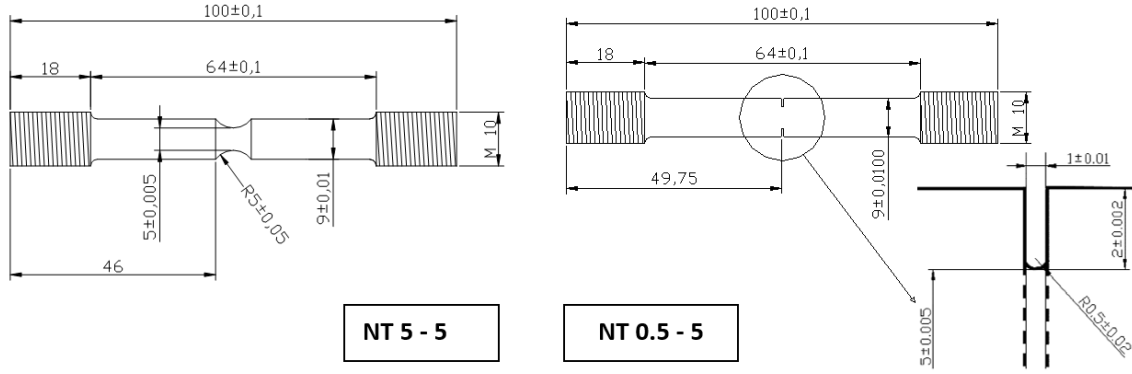


Figure 4. Geometries for axisymmetric notched cylindrical samples.

In order to reproduce the same environmental conditions that the ones employed for the aforementioned tests on C(T) specimens, two aspects must be taken into account. Respecting the applied intensities, the correspondence is direct, and the same current densities of 1, 5 and 10 mA/cm² must be used. But, in order to assure analogous local strain conditions in different geometries, different testing rates must be applied in each case. In both cases, as well as it was done for C(T) specimens, three identical local displacement conditions, V_{d1} , V_{d2} and V_{d3} , are applied, but the equivalent testing rates (in m/s) are different for each specimen geometry.

The local strain rates obtained in the C(T) specimens when applying the different displacement rates (V_{d1} , V_{d2} and V_{d3}) are obtained in the notched samples applying displacement rates different from the aforementioned ones, being also different for NT 0.5-5 and NT 5-5 geometries.

Therefore, to determine the relationship between rates, it is necessary to know the relationship that exists between the testing rate and the strain rate at the crack tip (C(T)) or notch tip (NT 0.5-5 and NT 5-5) for each type of specimen, in order to force them to be analogous. This procedure, detailed in [36], was done by using finite elements (FE) simulations and is summarised in Figure 5. It consists in obtaining a COD- ε graph from C(T) specimens (being ε the local deformation in the front of the crack/notch) and a δ - ε graph (being δ the CTOD) for each one of the notched axisymmetric geometries by FE (which slopes are the testing rates in each case). Then, imposing the same deformation increase in each geometry graph, $\Delta\varepsilon$, and assuring that takes place in the same time, the rates to be employed can be obtained by applying expressions (1) and (2). The correspondent rates obtained are presented in Table 5.

$$Rate_{NT0.5-5} = \frac{\Delta\delta_{NT0.5-5}}{\Delta COD} \cdot Rate_{C(T)} \quad (1)$$

$$Rate_{NT5-5} = \frac{\Delta\delta_{NT5-5}}{\Delta COD} \cdot Rate_{C(T)} \quad (2)$$

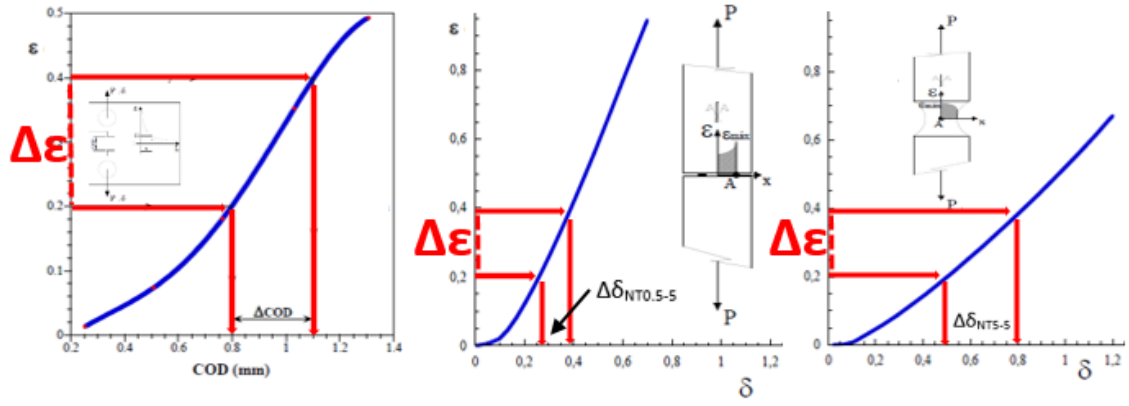
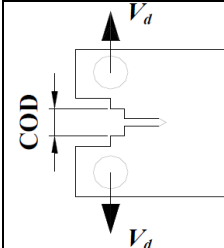
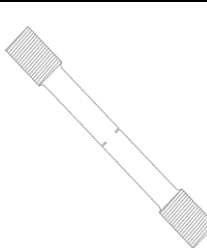
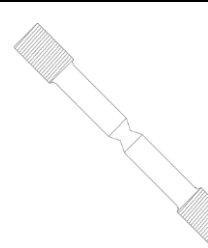


Figure 5. Schematic of the methodology to calculate equivalent testing rates.

Table 5. Summary of testing rates to be employed for the axisymmetric specimens.

| |  C(T) B=25mm |  NT 0.5 - 5 |  NT 5 - 5 |
|------------------------|--|---|--|
| V_{d-1} | 10 ⁻⁷ m/s | 0.17·10 ⁻⁷ m/s | 0.40·10 ⁻⁷ m/s |
| V_{d-2} | 10 ⁻⁸ m/s | 0.28·10 ⁻⁸ m/s | 0.68·10 ⁻⁸ m/s |
| V_{d-3} | 10 ⁻⁹ m/s | 0.38·10 ⁻⁹ m/s | 0.94·10 ⁻⁹ m/s |

4.2. Tensile tests experimental procedure and summary of test plan

The tests on axisymmetric specimens were carried out according to the recommendations of ISO 7539 [32], placing them in an electrolytic cell especially designed for this purpose, in such a way that the central part of the specimen was completely immersed inside the aqueous solution.

In order to avoid the formation of bubbles on the surface of the specimen and guarantee the continuous adsorption of hydrogen into the material, the liquid was stirred by a continuous small argon flow inside the cell; Figure 6 shows an schematic and a general view of the experimental set-up, where the counter electrode employed was a platinum wire rolled around the specimen.

Due to the impossibility to introduce an extensometer inside the solution, it was also necessary to implement an alternative. For this purpose, the authors of this work patented the methodology described in [37], that allows to continuously measure the specimen perimeter variation in the reduced net section during the test. A schematic of the device is presented in Figure 7.

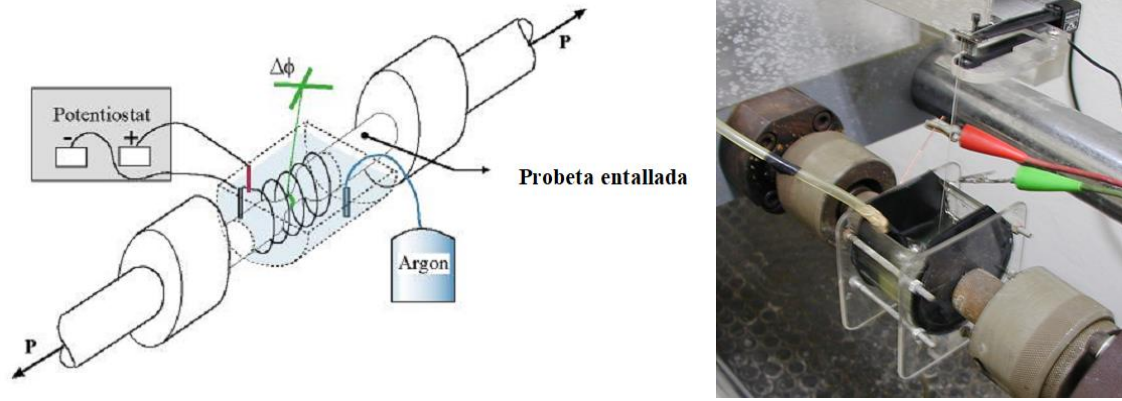


Figure 6. Schematic (left) and general view (right) of the experimental set-up.

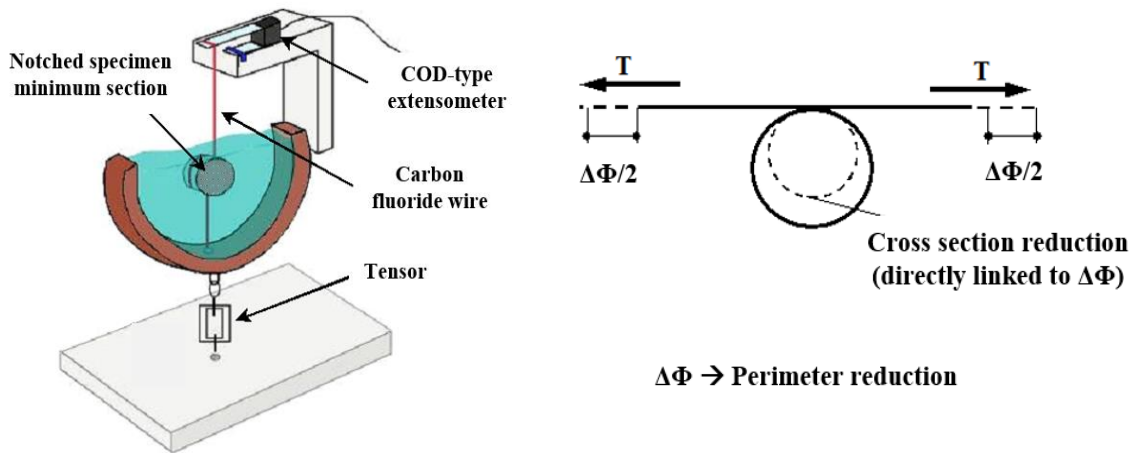
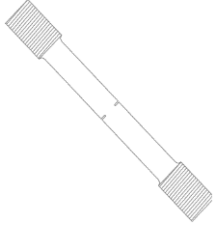
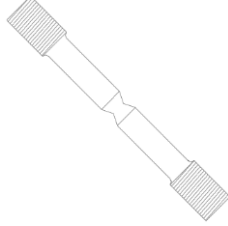


Figure 7. Schematics of the specimen perimeter variation measurement technique.

Prior to starting the test, the specimens were subjected to hydrogen absorption by exposing them for 24 hours to the environment, a time considered sufficient [38] for a proper and homogenous hydrogen distribution. After this, the slow strain rate test was started while the cathodic polarisation is applied simultaneously, being the direct results the load-perimeter variation register, $P-\Delta\Phi$, up to break, and the breaking section of the specimens analysed by SEM techniques.

Table 6 shows a summary of the test plan carried out following the methodology previously exposed. Firstly, tests without the influence of the environment, in air, were carried out for both geometries and materials, using in this case the fastest testing rate (as it has no influence when testing in air). Then, for both geometries, the three current densities of 1, 5 and 10 mA/cm² were employed to study the influence of the environment at the intermediate displacement rate (V_{d2}). Also, the rate influence was studied, performing tests at the three different displacement rates, V_{d1} , V_{d2} and V_{d3} , using in all the cases the environment of intermediate aggressiveness, 5 mA/cm².

Table 6. Summary of test plan

| X65 - 3Cr-1Mo-0.25V | | | | | |
|---|---------|-----------------------------|-----------------------------|------------------------------|---|
|  NT 0.5 - 5 | Air | I = 1 mA/cm ² | I = 5 mA/cm ² | I = 10 mA/cm ² |  NT 5 - 5 |
| $V_{d-1} \rightarrow 0.17 \cdot 10^{-7}$ m/s | - YES - | no | YES | no | $V_{d-1} \rightarrow 0.40 \cdot 10^{-7}$ m/s |
| $V_{d-2} \rightarrow 0.28 \cdot 10^{-8}$ m/s | no | YES | YES | YES | $V_{d-2} \rightarrow 0.68 \cdot 10^{-8}$ m/s |
| $V_{d-3} \rightarrow 0.38 \cdot 10^{-9}$ m/s | no | no | YES | no | $V_{d-3} \rightarrow 0.94 \cdot 10^{-9}$ m/s |

5. Experimental results

5.1. Samples tested in air from both steels

On Figure 8 the $P-\Delta\Phi$ registers of both materials and axisymmetric specimen geometries tested in air are presented, while the correspondent fractography is displayed on Figure 9.

It can be appreciated in both geometries, NT 0.5-5 and NT 5-5, that the 3Cr-1Mo-0.25V steel showed higher mechanical parameters than X65, as it was in their conventional characterisation (section 2.1). On the other hand, for both materials, the NT 0.5-5 notch specimens showed higher applied load than the NT 5-5, but less deformation capacity, indicating that for NT 5-5 it is not the notch root area the one that initiates the final failure, which is a result of the plastic collapse produced at the net section initiated in its centre by microvoids coalescence micromechanism, without any evident crack initiation generated by the notch. In all cases, ductile microvoids coalescence mechanisms were observed at the fracture surface.

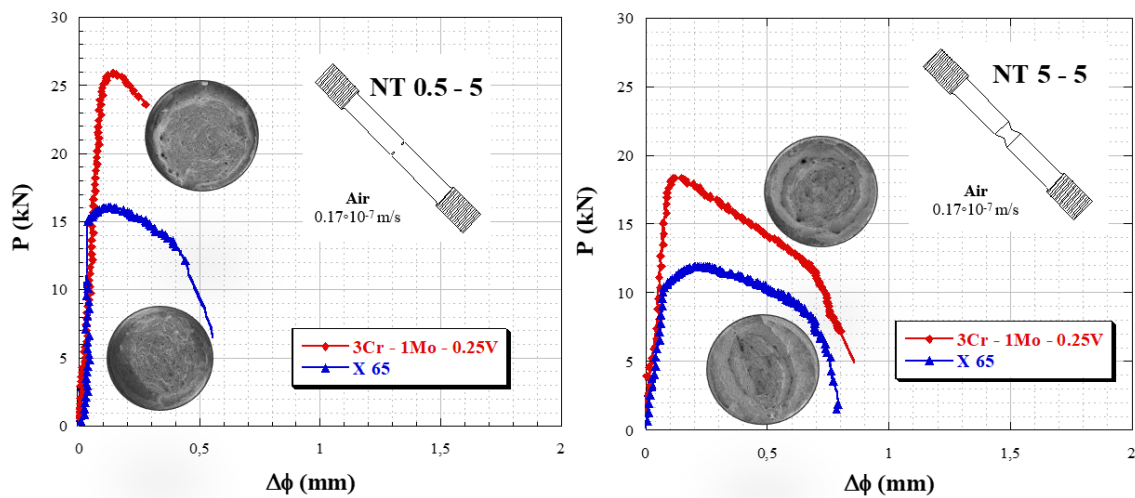


Figure 8. $P-\Delta\Phi$ registers of NT 0.5-5 and NT 5-5 specimens from X65 and 3Cr-1Mo-0.25V steels tested in air.

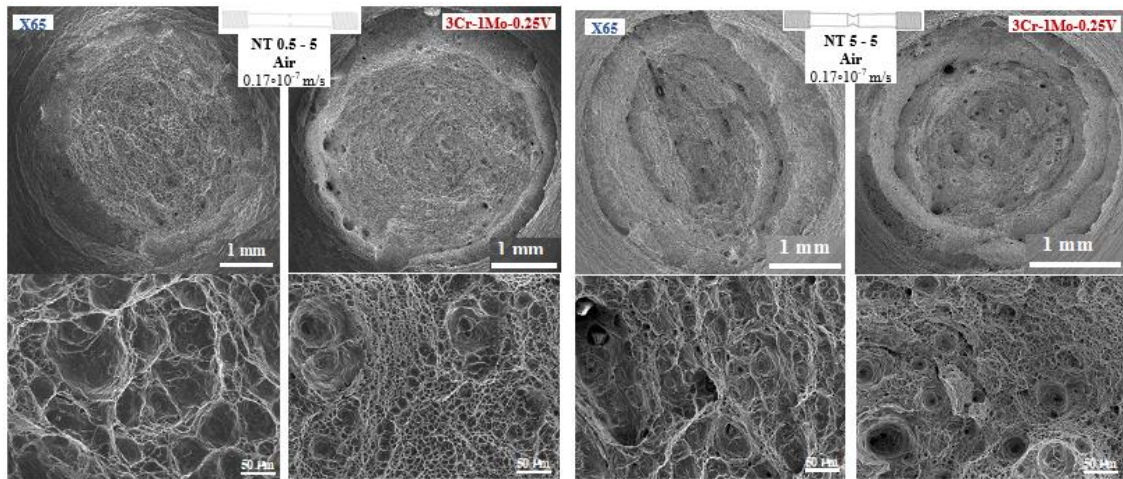


Figure 9. Fractography of NT 0.5-5 (left) and NT 5-5 (right) specimens from X65 and 3Cr-1Mo-0.25V steels tested in air.

5.2. X65 steel samples tested in environment

In Figure 10 the influence of the hydrogen in the behaviour obtained for the two geometries tested can be observed, while in Table 7 the maximum loads reached during the tests, P_{max} , are summarised. The upper row shows (NT 0.5-5 left and NT 5-5 right) the evolution of the behaviour when the aggressiveness varies (current densities of 1, 5 and 10 mA/cm²) for the same loading rate (intermediate displacement rate V_{d2}). The bottom row shows the rate impact (V_{d1} , V_{d2} and V_{d3} deformational rates) on the behaviour when the environment remains constant (intermediate current density of 5 mA/cm²). The loss of ductility is gradually observed in both notches with the increase in environment aggressiveness. For the sharper notches, NT 0.5-5, the hydrogen effect is very important for the two higher aggressive conditions (5 and 10 mA/cm²) leading to strength losses close to 50%. Meanwhile, for the blunter ones, NT 5-5, its main effect, with similar embrittlement percentage, appear just in the most aggressive condition (10 mA/cm²). A similar effect takes place with the rate influence. For the NT 0.5-5, sharper specimens, the displacement rate effect takes place from condition V_{d1} to V_{d2} , then stabilises. For the NT5-5, blunter specimens, a small and gradual embrittlement effect is obtained as the displacement rate decreases.

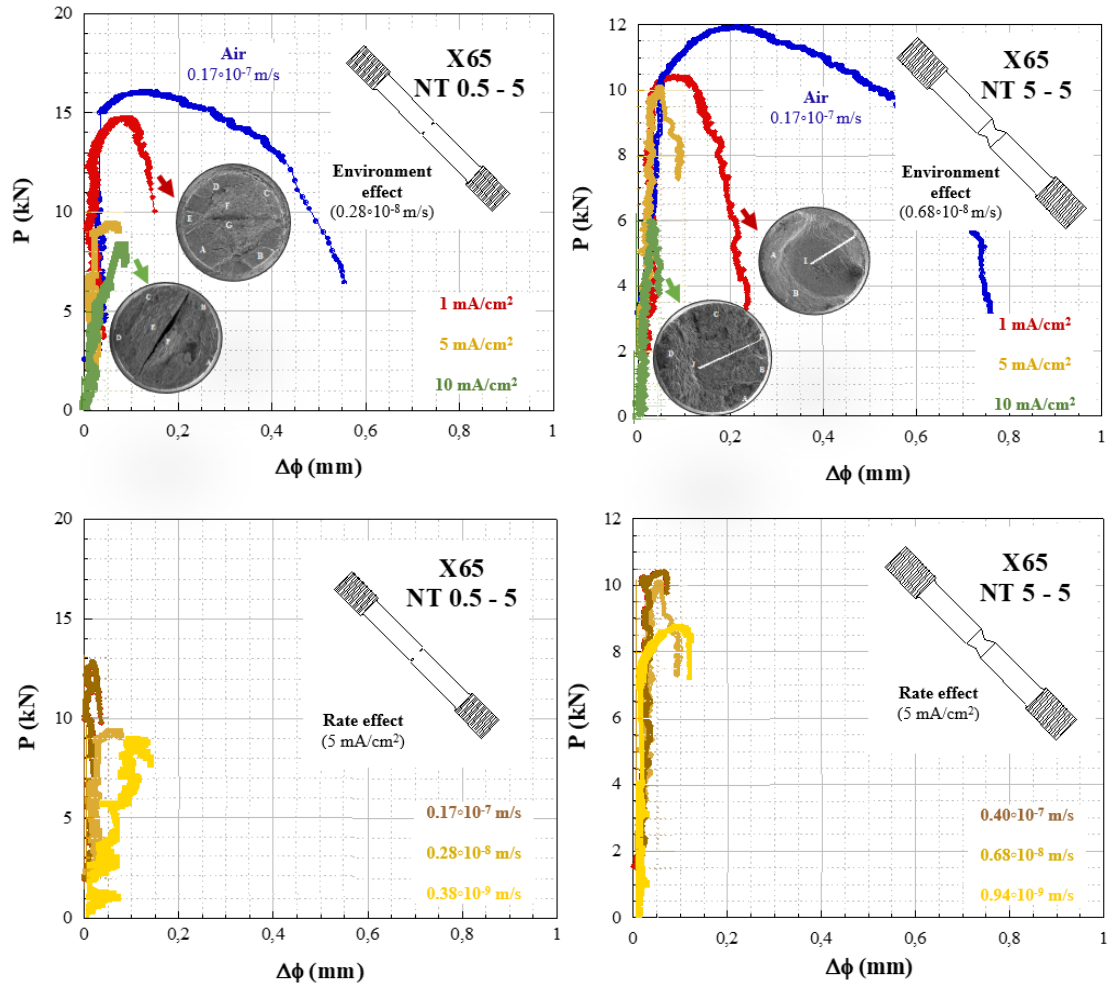


Figure 10. P - $\Delta\Phi$ registers of NT 0.5-5 and NT 5-5 specimens from X65 steel tested under the different environments and testing rates. Upper graphs: environment influence at constant deformational rate V_{d2} (excepting for the air at the fastest rate V_{d1}); Lower graphs: rate influence at constant environment of 5 mA/cm^2 .

Table 7. Maximum loads, P_{max} , reached during the axisymmetric tests in X65 steel. The colours employed correspond to the ones used in the P - $\Delta\Phi$ registers.

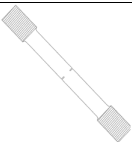
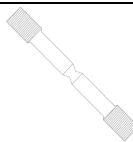
| X65 P_{max} (KN) NT 0.5 - 5 | | | |  |  | X65 P_{max} (KN) NT 5 - 5 | | | |
|-------------------------------------|---------------------------|---------------------------|----------------------------|---|---|-----------------------------------|---------------------------|---------------------------|----------------------------|
| Air | I = 1 mA/cm^2 | I = 5 mA/cm^2 | I = 10 mA/cm^2 | | | Air | I = 1 mA/cm^2 | I = 5 mA/cm^2 | I = 10 mA/cm^2 |
| 16.0 | - | 12.9 | - | V_{d-1} (m/s) $0.17 \cdot 10^{-7}$ | V_{d-1} (m/s) $0.40 \cdot 10^{-7}$ | 11.8 | - | 10.4 | - |
| - | 14.9 | 9.4 | 8.5 | V_{d-2} (m/s) $0.28 \cdot 10^{-8}$ | V_{d-2} (m/s) $0.68 \cdot 10^{-8}$ | - | 10.5 | 10.1 | 6.0 |
| - | - | 9.1 | - | V_{d-3} (m/s) $0.38 \cdot 10^{-9}$ | V_{d-3} (m/s) $0.94 \cdot 10^{-9}$ | - | - | 8.8 | - |

Figure 11 shows the fracture surfaces of the NT 0.5-5, sharper specimens, tested at 1 mA/cm^2 (top) and 10 mA/cm^2 (bottom) at the intermediate deformational rate V_{d2} . In the least embrittled specimen (1 mA/cm^2), with a maximum load around 10% lower than the one in air, a subcritical propagation process appeared, the crack propagates in almost all

the periphery of the specimen through tearing-like mechanisms with some cleavages, lower than 1 mm. The final rupture occurs at the centre through plastic instability, associated to microvoid formation and coalescence. In the most embrittled behaviour (10 mA/cm²), where the failure occurred at a maximum load of around 50% of the corresponding load when tested at air, a mixture of tearing-like and quasi-cleavage cracking micromechanisms, is observed on the periphery. After the brittle propagation in this zone, a final rupture through instability of the residual ligament in the centre of the specimen happens, cleavage being due to the high hydrogen presence, surrounded by more ductile areas.

In the same way, Figure 12 shows the fracture surfaces of the NT 5-5, blunter specimens, tested at 1 mA/cm² (top) and 10 mA/cm² (bottom) at the intermediate deformational rate V_{d2} . At the least aggressive case (1 mA/cm²), an internal fracture is previously obtained associated to low strained microvoids in the centre of the specimen, followed by ductile shearing lips on the periphery. In this case, the failure occurs after a maximum load around 10% lower than the one tested in air. At the most aggressive conditions (10 mA/cm²), the high hydrogen presence promotes different areas of fracture, like facets, in all of them associated to brittle quasi cleavage fracture zones. In this case, hydrogen effect, noticeable in terms of ductility, represents an embrittlement for which the maximum load reached around 50% of the one in air.

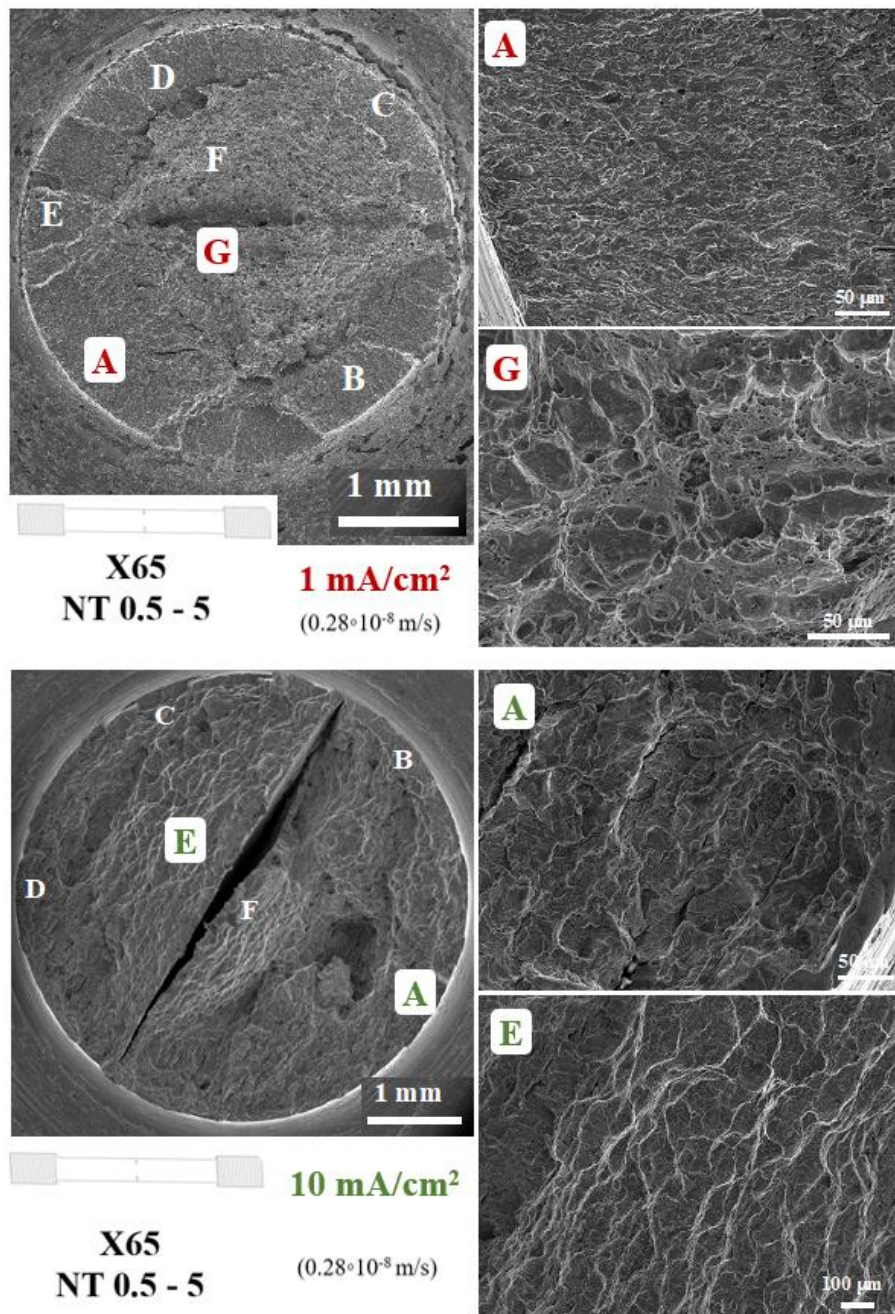


Figure 11. Fractography of NT 0.5-5 specimens from X65 steel tested at intermediate deformational rate, V_{d2} . Upper: least aggressive environment, 1 mA/cm²; Lower: most aggressive environment 10 mA/cm².

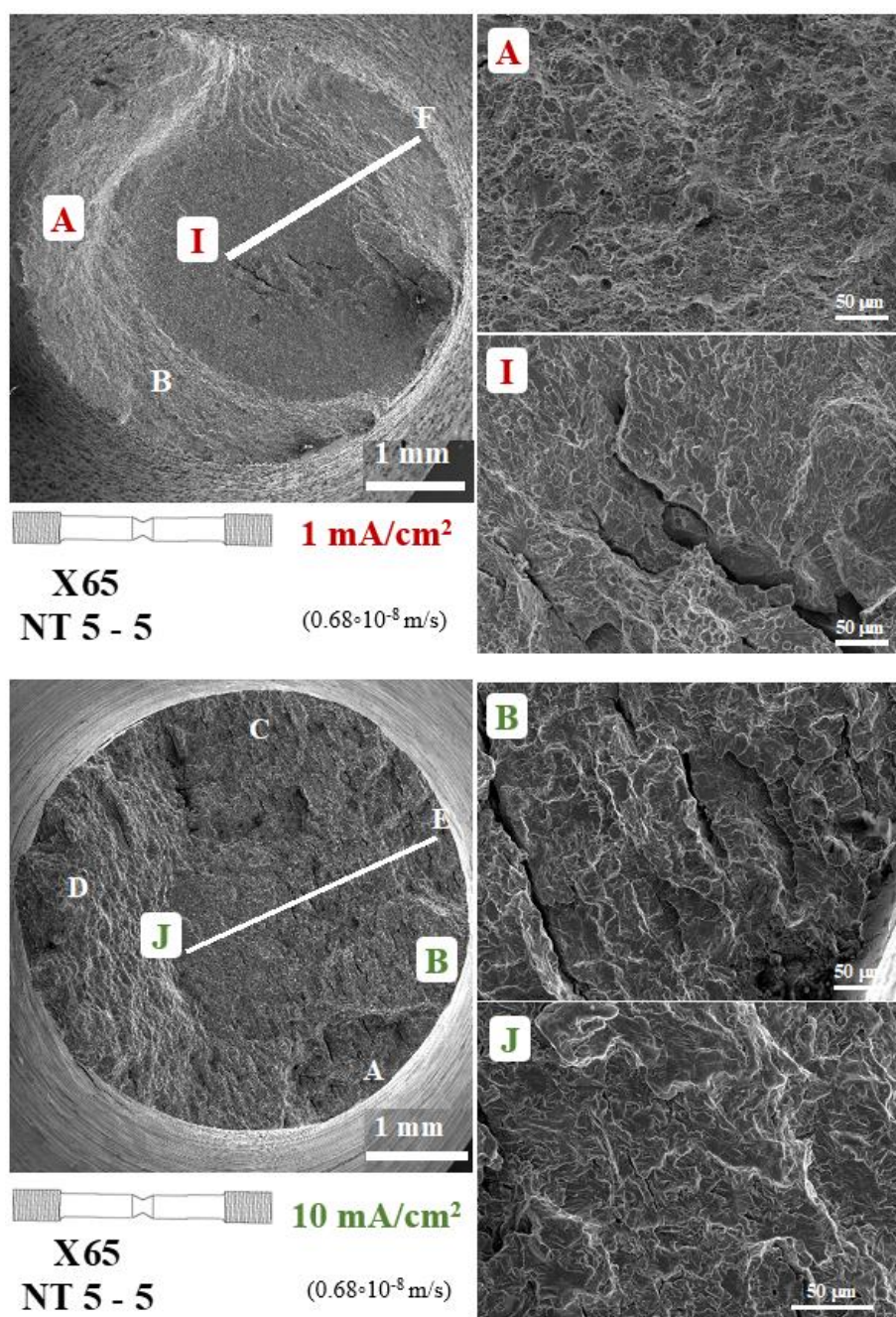


Figure 12. Fractography of NT 5-5 specimens from X65 steel tested at intermediate deformational rate, V_{d2} . Upper: least aggressive environment, 1 mA/cm²; Lower: most aggressive environment 10 mA/cm².

5.3. 3Cr-1Mo-0.25V steel samples tested in environment

Figure 13 shows the influence of the hydrogen in the behaviour obtained for the two geometries tested for 3Cr-1Mo-0.25V steel, while in Table 8 the maximum loads reached during the tests, P_{max} , are summarised. The upper row shows (NT 0.5-5 at left and NT 5-5 at right) the evolution of the behaviour when the aggressiveness varies (current densities of 1, 5 and 10 mA/cm²) for the same loading rate (intermediate displacement rate V_{d2}). The bottom row shows the rate impact (V_{d1} , V_{d2} and V_{d3} displacement rate conditions) on the behavior when the environment remains constant (intermediate environment of 5 mA/cm²). The loss of ductility is very marked in the sharper notches, NT 0.5-5, increasing with aggressiveness up to a loss of strength of 65%. Nevertheless for the blunter ones, NT 5-5, the hydrogen effect, loss of ductility, is only appreciated for the higher aggressive conditions (5 and 10 mA/cm²). With reference to the displacement rate effect, at the sharper notch specimens, only the slower rate offered an increased effect over the already important environmental effect. At the blunter ones the displacement rate effect is still noted, but much more reduced.

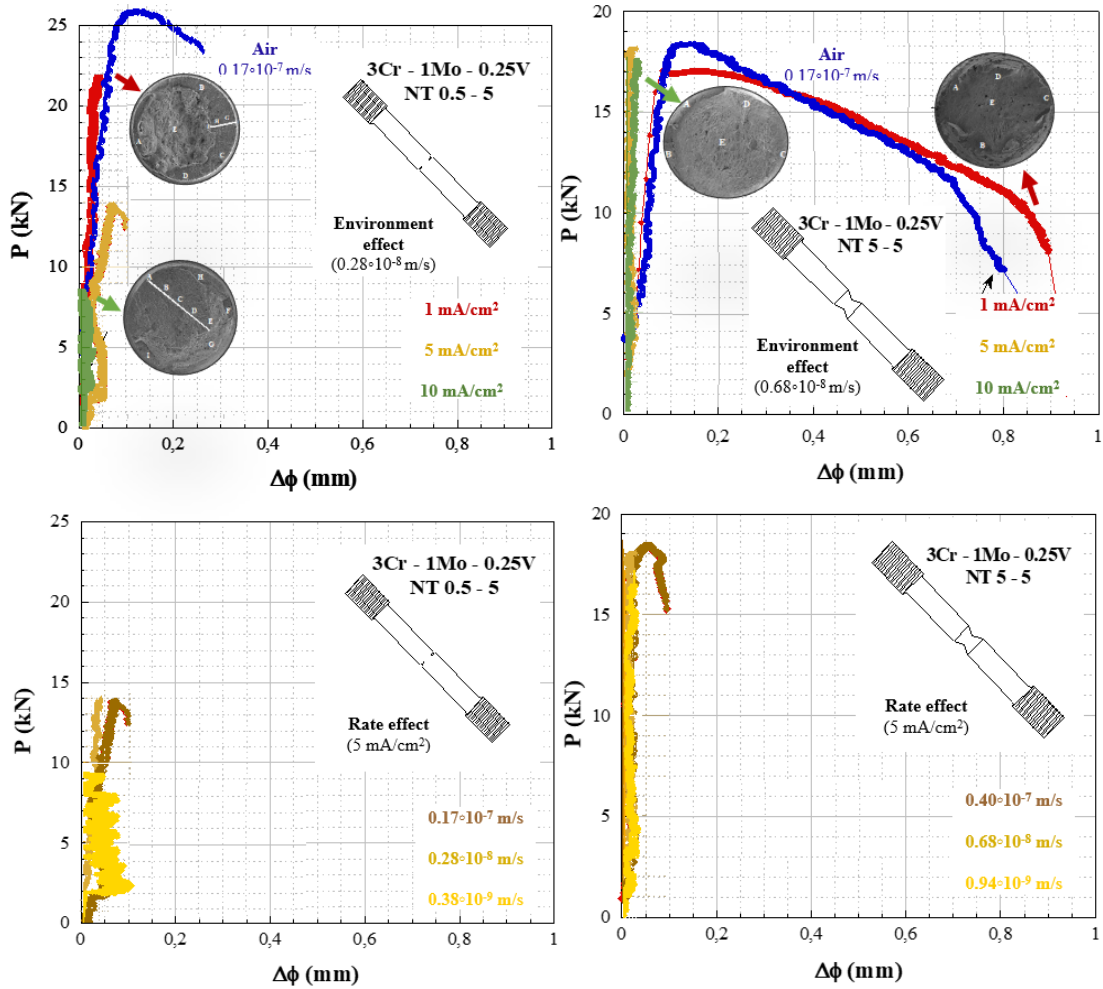


Figure 13. $P-\Delta\Phi$ registers of NT 0.5-5 and NT 5-5 specimens from 3Cr-1Mo-0.25V steel tested under the different environments and testing rates. Upper graphs: environment influence at constant deformational rate V_{d2} (excepting for the air

at the fastest rate V_{d1}); Lower graphs: rate influence at constant environment of 5 mA/cm^2 .

Table 8. Maximum loads, P_{max} , reached during the axisymmetric tests in 3Cr-1Mo-0.25V steel. The colors employed correspond to the ones used in the $P-\Delta\Phi$ registers.

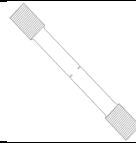
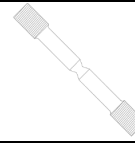
| 3Cr-1Mo-0.25V P_{max} (KN) NT 0.5 - 5 | | | |  |  | 3Cr-1Mo-0.25V P_{max} (KN) NT 5 - 5 | | | |
|---|---------------------------|---------------------------|----------------------------|---|---|---|---------------------------|---------------------------|----------------------------|
| Air | I = 1 mA/cm^2 | I = 5 mA/cm^2 | I = 10 mA/cm^2 | | | Air | I = 1 mA/cm^2 | I = 5 mA/cm^2 | I = 10 mA/cm^2 |
| 25.8 | - | 14.0 | - | V_{d-1} (m/s) $0.17 \cdot 10^{-7}$ | V_{d-1} (m/s) $0.40 \cdot 10^{-7}$ | 18.5 | - | 18.5 | - |
| - | 21.9 | 14.0 | 8.8 | V_{d-2} (m/s) $0.28 \cdot 10^{-8}$ | V_{d-2} (m/s) $0.68 \cdot 10^{-8}$ | - | 17.0 | 18.0 | 17.5 |
| - | - | 9.2 | - | V_{d-3} (m/s) $0.38 \cdot 10^{-9}$ | V_{d-3} (m/s) $0.94 \cdot 10^{-9}$ | - | - | 16.6 | - |

Figure 14 shows the fracture surfaces of the NT 0.5-5, sharper specimens, tested at 1 mA/cm^2 (top) and 10 mA/cm^2 (bottom) at the intermediate displacement rate V_{d2} . In the least embrittled specimen (1 mA/cm^2), reaching a maximum load around 20% lower than the one in air, a subcritical crack propagation process appeared initially: the crack propagates up to 1mm in some cases in almost all the periphery of the specimen through tearing-like mechanisms with some cleavages. The final rupture occurs at the centre trough plastic instability, associated to microvoid coalescence formation. In the most embrittled behavior (10 mA/cm^2), the failure occurred at a maximum load of 8.8 kN (around 35% of the corresponding load when tested at air). At the periphery, again, a mixture tearing-like and cleavage cracking micromechanisms, is observed suggesting subcritical initial cracking. After the brittle propagation in this zone, leads to a final rupture through instability of the residual ligament in the centre of the specimen that breaks by forming microvoids around cleavage cracked areas due to the higher embrittlement produced by hydrogen presence.

Figure 15 shows the fracture surfaces of the NT 5-5, blunter specimens, tested at 1 mA/cm^2 (top) and 10 mA/cm^2 (bottom) at the intermediate deformational rate V_{d2} . At the least aggressive case (1 mA/cm^2), an internal fracture is previously obtained associated to low strained microvoids in the centre of the specimen, followed by ductile shearing lips at the periphery. As previously stated, hydrogen has practically no effect at all when compared with the sample tested in air. At the most aggressive conditions (10 mA/cm^2), the high hydrogen presence promotes fracture with almost no ductility and a final rupture. In this case, hydrogen effect was noticeable in terms of ductility, but the maximum load reached was not far from the one in air.

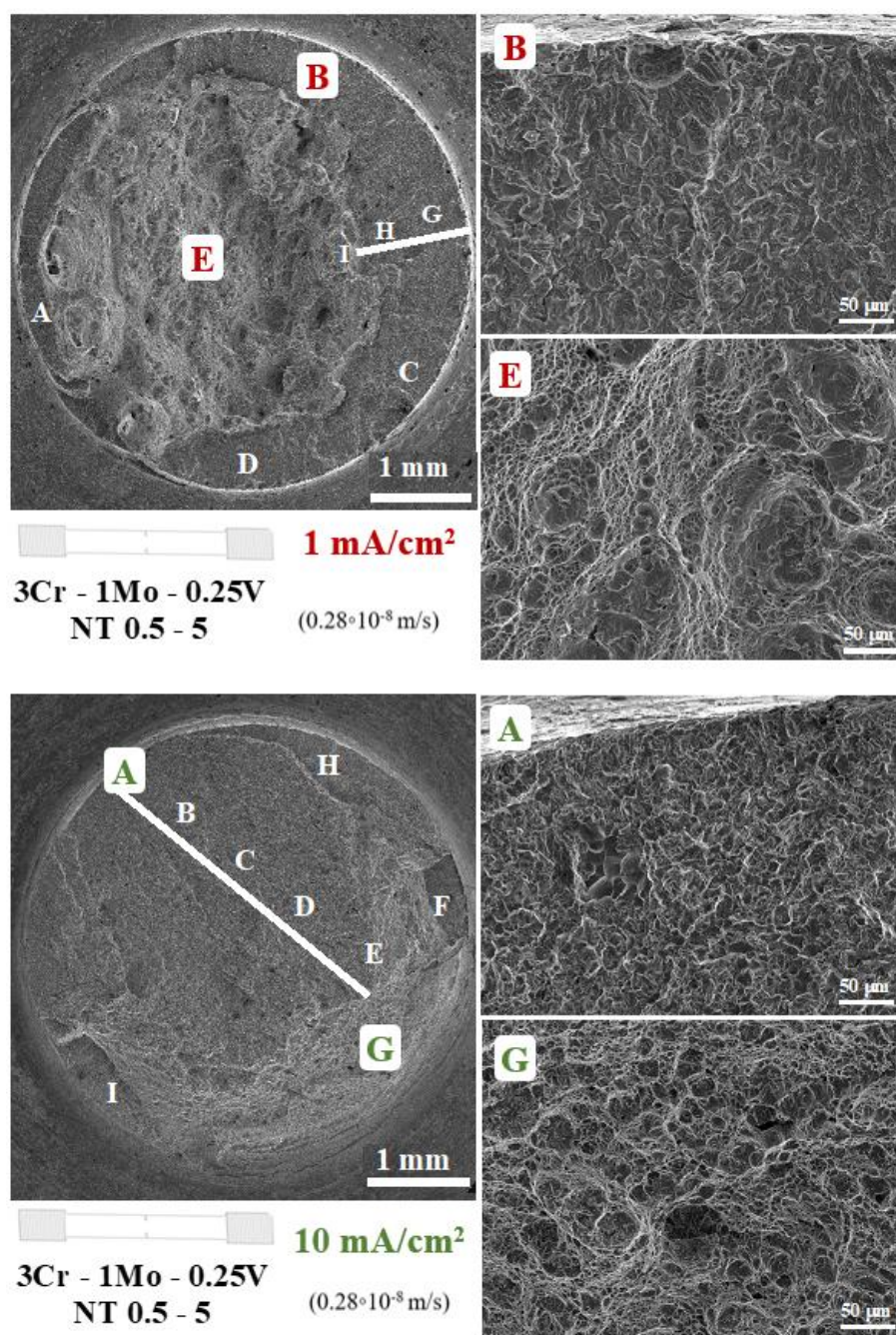


Figure 14. Fractography of NT 0.5-5 specimens from 3Cr-1Mo-0.25V steel tested at intermediate deformational rate, V_{d2} . Upper: least aggressive environment, 1 mA/cm^2 ; Lower: most aggressive environment 10 mA/cm^2 .

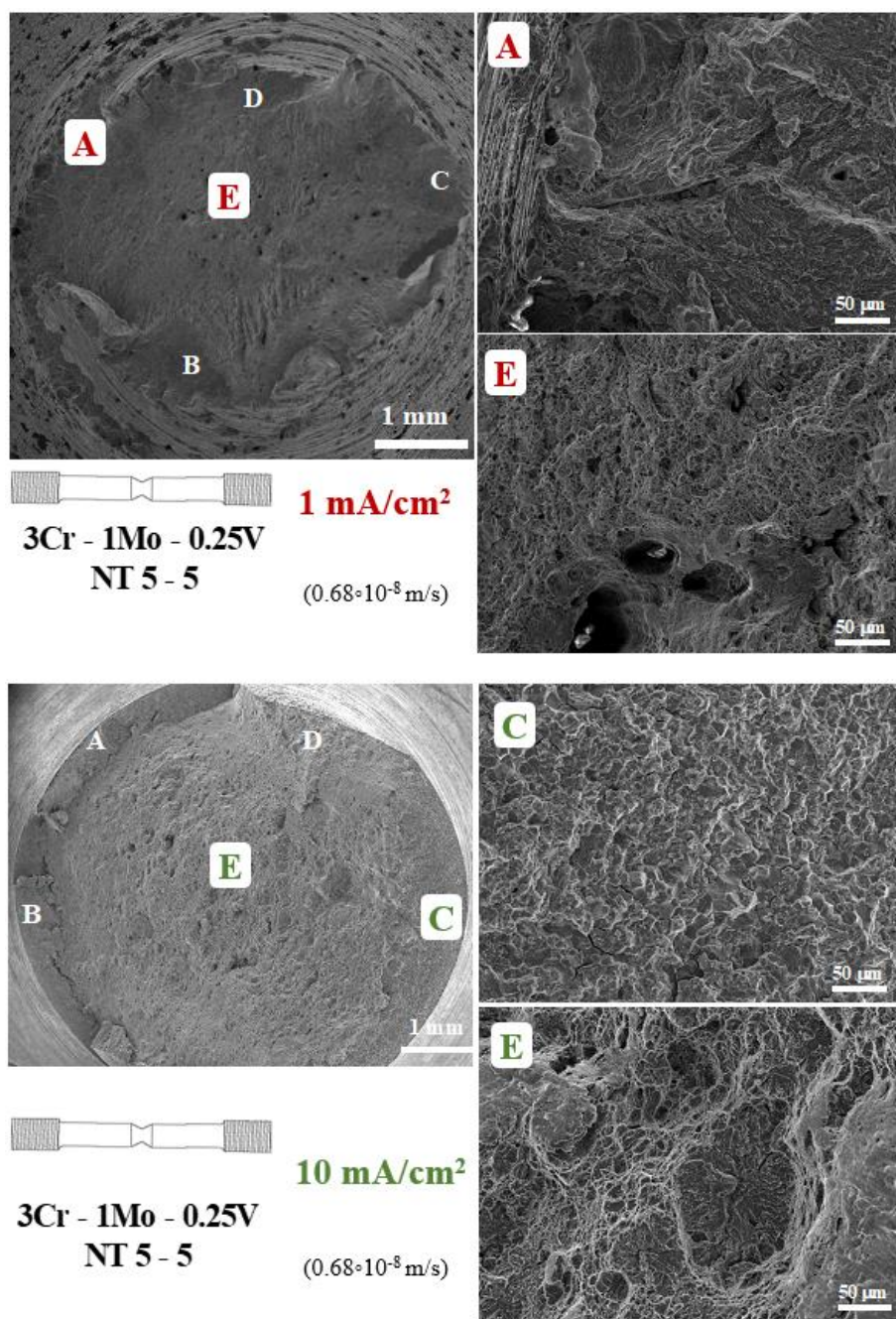


Figure 15. Fractography of NT 5-5 specimens from X65 steel tested at intermediate deformational rate, V_{d2} . Upper: least aggressive environment, 1 mA/cm^2 ; Lower: most aggressive environment 10 mA/cm^2 .

6. Analysis of the results

6.1. Hydrostatic stress and equivalent plastic deformation to explain the Hydrogen embrittlement processes up to fracture

Once the tests results had been presented, and their fractographic aspects analysed, a FE analysis was carried out in order to evaluate the stress and strain levels on a local scale in the minimum notched section of the specimen at the moment of the instability ~~is carried out~~.

Figure 16 and Figure 17 present, for X65 and 3Cr-1Mo-0.25V respectively, the results obtained from the aforementioned analysis in terms of hydrostatic stress, σ_h , and equivalent plastic deformation, ϵ_p , along the radius of the minimum notched section for both types of geometries at the moment of the specimen failure. To allow a comparison between the hydrostatic stress state in both materials, this parameter is presented as its ratio over the material yield stress, σ_h/σ_y . For both materials and both sample geometries, the environmental effect has been analysed by comparing the results of samples tested at the intermediate displacement rate.

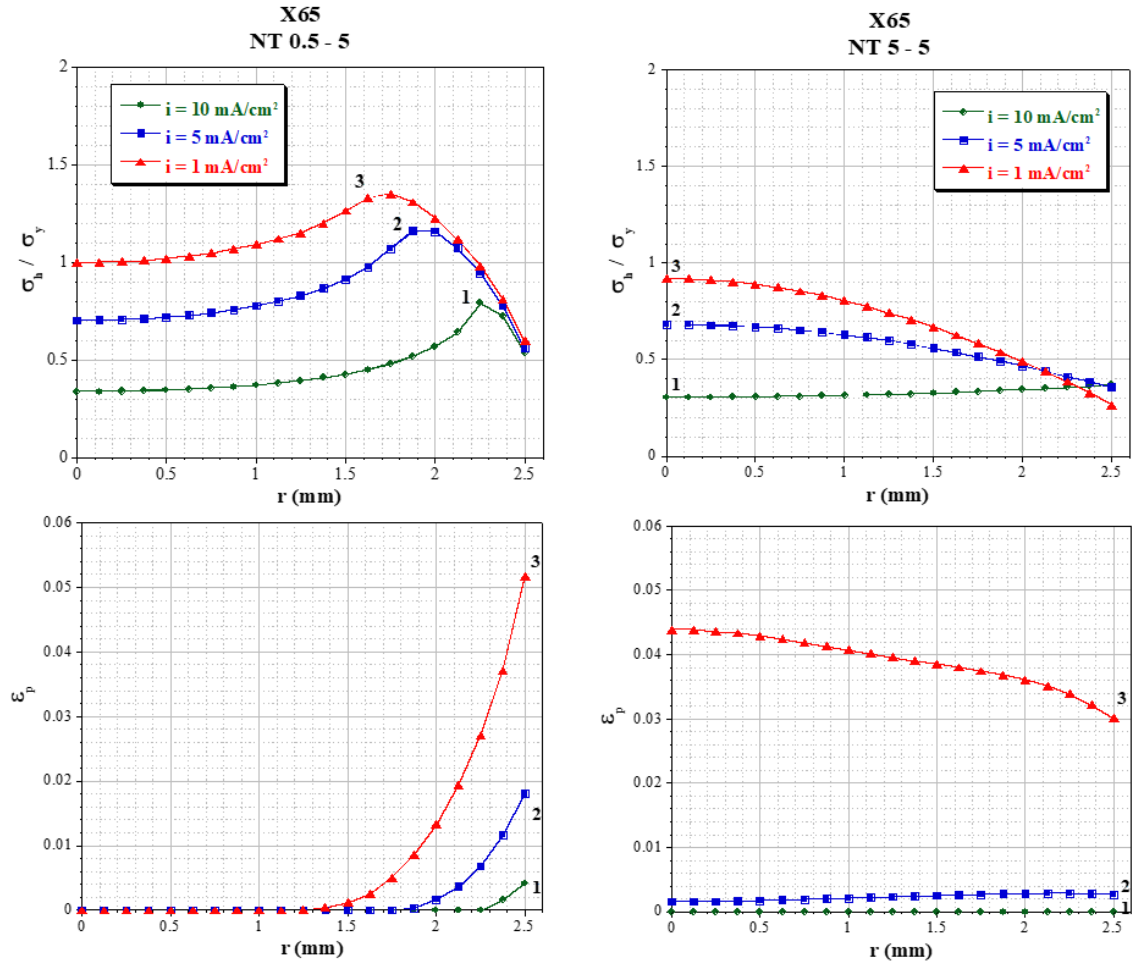


Figure 16. Hydrostatic stress (up) and plastic strain (bottom) profiles along the radius of the neck section of NT 0.5-5 (left column) and NT 5-5 (right column) FE simulations from X65 steel under the different environments under their instability loads. The centre of the specimen is $r=0$ and the periphery $r=2.5$ mm.

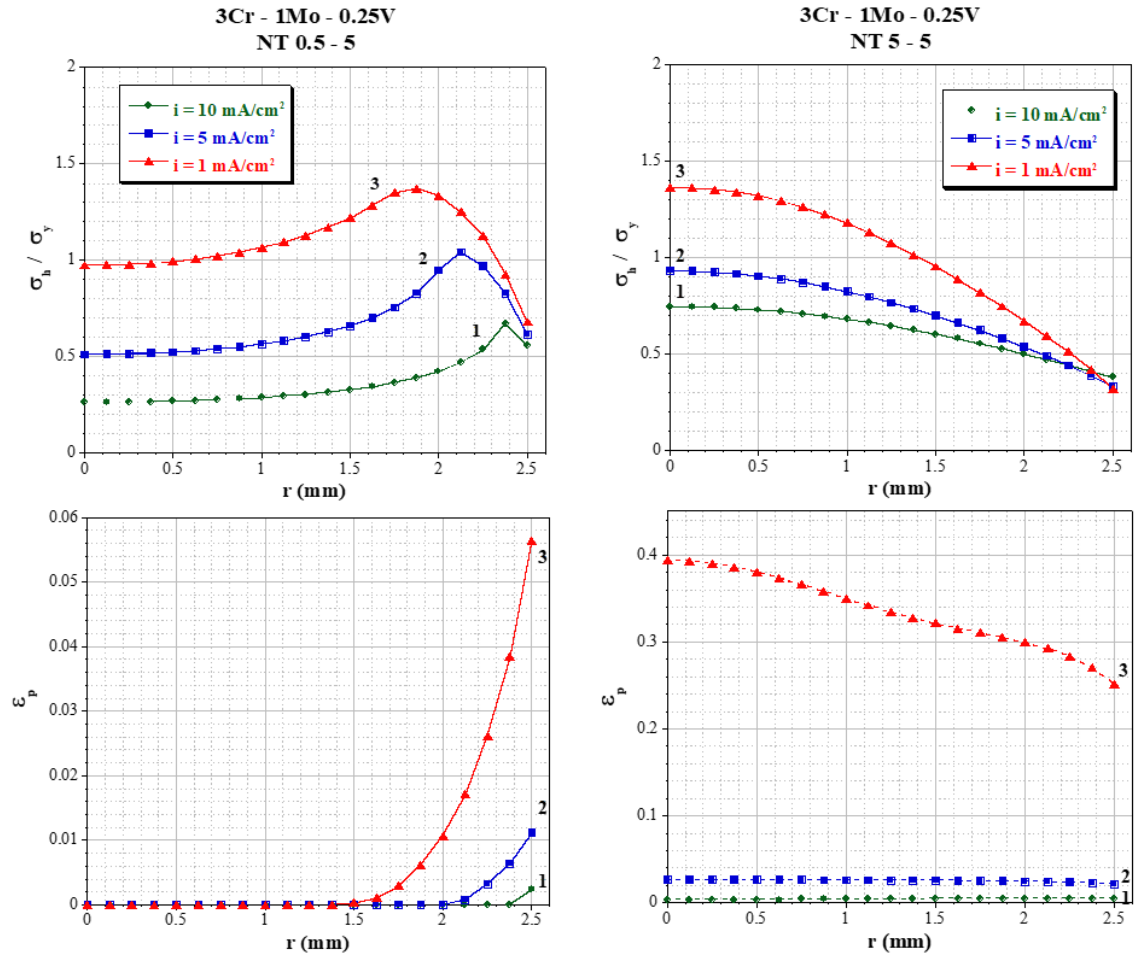


Figure 17. Hydrostatic stress (up) and plastic strain (bottom) profiles for the neck section of NT 0.5-5 (left column) and NT 5-5 (right column) FE simulations from 3Cr-1Mo-0.25V steel under the different environments under their instability loads. The centre of the specimen is $r=0$ and the periphery $r=2.5$ mm.

In the left column of Figure 16, corresponding to X65 steel for the sharper notch (NT 0.5-5), it can be observed how the maximum value of the hydrostatic stress, σ_h , takes place near the surface of the notch for all the environments, and gets reduced towards the centre of the section. The more aggressive the environment is, the closer this maximum σ_h is to the surface (at 0.75mm, 0.65mm and 0.35mm for 1, 5 and 10 mA/cm² respectively). σ_h value is over the yield stress for the less aggressive environments (1 and 5 10 mA/cm²) while its value reduces to around 80% of σ_y for 10 mA/cm². Simultaneously, for NT 0.5-5 on X65, the maximum equivalent plastic strain value, ϵ_p , takes place at the surface of the notch for all the environments, but reaches a very low value in all cases (0.052, 0.018 and 0.004 for 1, 5 and 10 mA/cm² respectively) if compared to X65 strain at maximum load of 0.147 (see Table 2), indicating the important increasing embrittling effect of hydrogen, as it reduces the strain needed for initiate subcritical cracking processes [22] [23]. This fact proves that the existence of a moderate value of hydrostatic stress close to the surface is attracting to hydrogen presence at this area and, once the local strain reaches the critical one defined by the embrittlement conditions due to hydrogen concentration, subcritical annular cracking appears from the notch. If the three environments are

compared, it can be seen that for 1 mA/cm² (least aggressive) the critical plastic deformation is the highest, and the lower hydrogen activity concentration requires the highest level of the hydrostatic stress σ_h , to reach the critical situation. This combined situation gradually evolves to the opposite when the hydrogen concentration is maximum for 10mA/cm².

In the right column of Figure 16, corresponding to X65 steel for the blunter notch (NT 5-5), it can be observed how the maximum value of the hydrostatic stress, σ_h , takes place in the centre of the section, and gets reduced to a similar value on the periphery in the three environments. This justifies that the zone towards hydrogen diffuses is the centre of the sample transversal section and means that hydrogen must have diffused up there. In this geometry, the maximum hydrostatic stresses, σ_h , are in all the cases lower than their homologous for the sharper one, lower than the yield stress for all the environments, although for the least aggressive (1 mA/cm²) is very close to it, and also the more aggressive the environment, the lower the maximum hydrostatic stress. On the other hand, for NT 5-5 on X65, the equivalent plastic deformation value, ϵ_p , is fairly uniform along the radius, and also in this geometry does not reach a significant value in any environment; it is around 0.04 for 1 mA/cm² and practically inexistent in the rest. Those profiles of both, σ_h and ϵ_p variables, justify the differences observed in the fracture surfaces shown in Figure 12.

Regarding 3Cr-1Mo-0.25V hydrostatic stress, σ_h , and equivalent plastic strain, ϵ_p , along the radius of both geometries, displayed in Figure 17, the general characteristics observed and commented for X65 steel also take place in almost all the cases, with only a particular difference. For the sharper notch, NT 0.5-5 (left column from Figure 17), the maximum value of the hydrostatic stress, σ_h , takes place near the periphery for all the environments, and gets reduced towards the centre of the section. The maximum equivalent plastic deformation value, ϵ_p , also takes place at the surface of the notch, but in any case reaches a significant value compared with the one obtained from the test in air. That justifies the mechanical, cracking and fracture behavior, Figure 13 and Figure 14, obtained for these samples.

For the blunter notch, NT 5-5 (right column from Figure 17), the maximum value of the hydrostatic stress, σ_h , takes place in the centre of the section and gets reduced to a similar value on the periphery in the three environments. The equivalent plastic strain value, ϵ_p , is fairly uniform along the radius, and does not reach a significant value in the two most aggressive conditions. However, it must be pointed, as a different response, that for the least aggressive test condition, the maximum σ_h and ϵ_p are much higher than in the rest of the cases, probably suggesting that the lower aggressiveness of this environmental condition does not promote enough hydrogen entry to saturate the existent traps, then higher loading conditions are needed to increase the hydrostatic stress to attract more hydrogen, then promoting higher strain conditions and, finally, reaching critical conditions very close to those established in air. In fact, in Figure 13 can be observed that both P- $\Delta\phi$ registers, in air and in 1 mA/cm², are practically coincident, reaching very close maximum loads and strain values. This means that the hydrogen damage for this environmental condition is practically inexistent, which implies a fully plastic collapse of the whole section without any sign of embrittlement, as shown in Figure 15.

Once the hydrostatic stress and plastic strain profiles are known, it must be pointed that, in all the tested conditions analysed, they justify the different observed mechanical, cracking and fracture behaviours affected by hydrogen presence. Such explanation is supported at the end by the local level of hydrogen concentration, that follows [21] the expression:

$$C_H = \phi \cdot C_0 \cdot \exp \left[\frac{V^* \cdot \sigma_h}{RT} \right] (1 + \alpha \cdot \varepsilon_p) \quad (3)$$

where C_H is the local hydrogen level, ϕ is the hydrogen activity, C_0 is a reference concentration, V^* is the activation volume, R the universal gas constant, α is an adequate constant, and σ_h and ε_p are the hydrostatic stress and the plastic strain respectively. According to this expression (3), the zones where the value of σ_h and ε_p make maximum the value of hydrogen concentration will activate more brittle mechanisms of cracking and fracture, as it has been consequently observed.

This situation can justify, as a general rule the cracking processes observed for the sharpest notched NT 0.5-5 specimens, initiated at their external part, as a circular crown, followed by the plastic instability of the residual ligament. The highest strains at the surface and the maximum of the hydrostatic stresses near it allow the observed initial cracking processes on the periphery. As the aggressiveness increases (higher C_0), the local critical conditions are achieved with lower hydrostatic stresses and plastic strain, so for lower loads. Also more brittle cracking mechanisms, associated to lower strains, and higher hydrogen, are present.

Although for the blunter notch specimens NT 5-5, the higher strain and hydrostatic stress are at the centre, and their differences in profile and absolute values justify in all the cases the observed behavior.

6.2. Fracture toughness determination from tests on axysimetric NT 0.5-5 specimens

From the previous analysis, the sharper geometry, NT 0.5-5, with a sharpest notch could be studied under the precepts of fracture mechanics after the initiation of a subcritical cracking process, and the obtained results to be compared with those obtained for C(T) specimens and described in section 3 as a reference. A similar study is not applicable for the blunter notched specimens, NT 5-5, as their failures are in general not based on critical fracture conditions.

This means that the fracture toughness for the final failure, K_{I-HC} , in NT 0.5-5 must be related to the maximum load of the axisymmetric test, P_{max} , which also leads to the final failure. In order to quantify this, solutions for the stress intensity factor calculation in function of different geometries are given in codes such as BS 7910:2013 [39], which proposes the following formulation once simplified for NT 0.5-5 geometry uniaxially loaded:

$$K_I = M_m \cdot P_m \cdot \sqrt{\pi \cdot a} \quad (4)$$

Where the coefficient M_m is defined by (5);

$$M_m = \frac{r^{1.5}}{2(r-a)^{1.5}} \left\{ 1 + 0.5 \left(\frac{r-a}{r} \right) + 0.375 \left(\frac{r-a}{r} \right)^2 - 0.363 \left(\frac{r-a}{r} \right)^3 + 0.731 \left(\frac{r-a}{r} \right)^4 \right\} \quad (5)$$

P_m is the membrane stress of the specimen's shaft at P_{max} , calculated as its value over the $\phi 9$ mm section, and the flaw size "a" is equal to the machined notch on the sample, of 2 mm, plus the peripheral circumferential crown crack defined by its equivalent value. As these subcritical annular cracks, some of them collected in Figure 11 to Figure 15, had any regular growth of the crack front, an equivalent flaw size "a", used in the subsequent analysis, was obtained.

The technique employed for this purpose is schematised in Figure 18, and consisted in assimilating the real area on the fracture surface to an equivalent circular one centred in the $\phi 9$ mm specimen shaft. The flaw size for the calculations is then obtained adding the 2 mm machined notch to the width of equivalent circular centred crown. Table 9 collects the final equivalent flaw sizes "a" employed in further calculations.

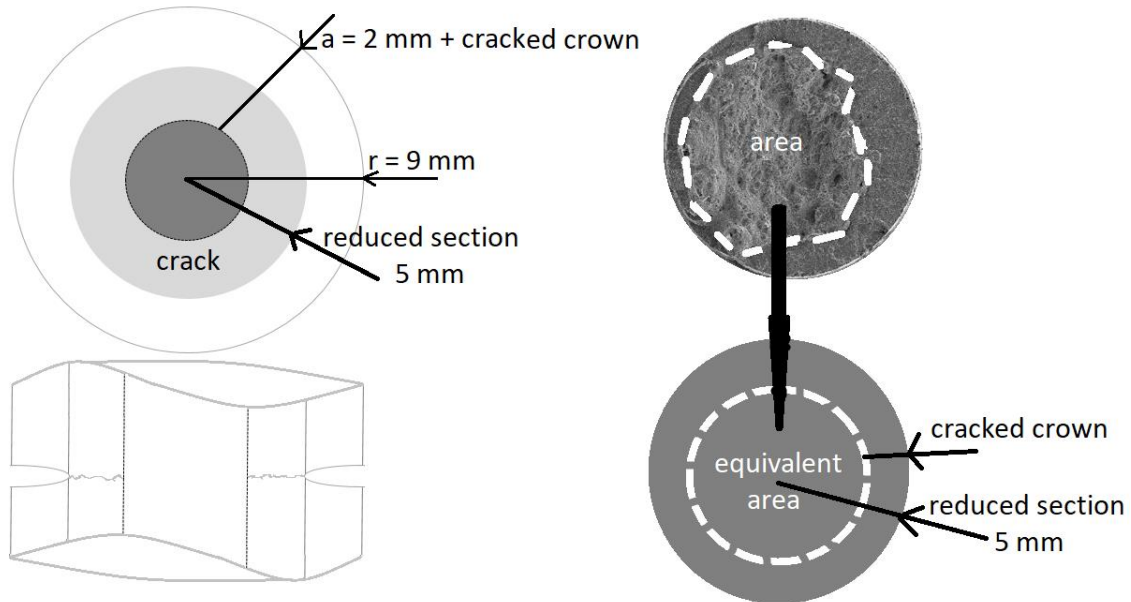



Figure 18. Definition of flaw size "a".

Table 9. Equivalent flaw sizes "a" in both steels for NT 0.5-5.

| X65 Equivalent flaw size "a" (mm) NT 0.5 - 5 | | |  | 3Cr-1Mo-0.25V Equivalent flaw size "a" (mm) NT 0.5 - 5 | | |
|--|-----------------------------|------------------------------|---|--|-----------------------------|------------------------------|
| I = 1 mA/cm ² | I = 5 mA/cm ² | I = 10 mA/cm ² | | I = 1 mA/cm ² | I = 5 mA/cm ² | I = 10 mA/cm ² |
| - | 3.17 | - | V_{d-1} (m/s) $0.40 \cdot 10^{-7}$ | - | 3.17 | - |
| 2.79 | 3.03 | 1.15 | V_{d-2} (m/s) $0.68 \cdot 10^{-8}$ | 2.89 | 3.11 | 2.97 |
| - | 3.07 | - | V_{d-3} (m/s) $0.94 \cdot 10^{-9}$ | - | 3.19 | - |

By applying the aforementioned formulation, and the aforementioned equivalent flaw sizes, values of K_{I-HC} can be estimated from each one of the tests performed on

axisymmetric specimens and compared to the results on C(T) specimens presented in section 3. It can be observed that in all the cases the estimations are in the $\pm 15\%$ error interval, good enough considering the simplified method used to determine those values. And good enough to validate the existence of HIC processes previous to final brittle fracture due to hydrogen presence.

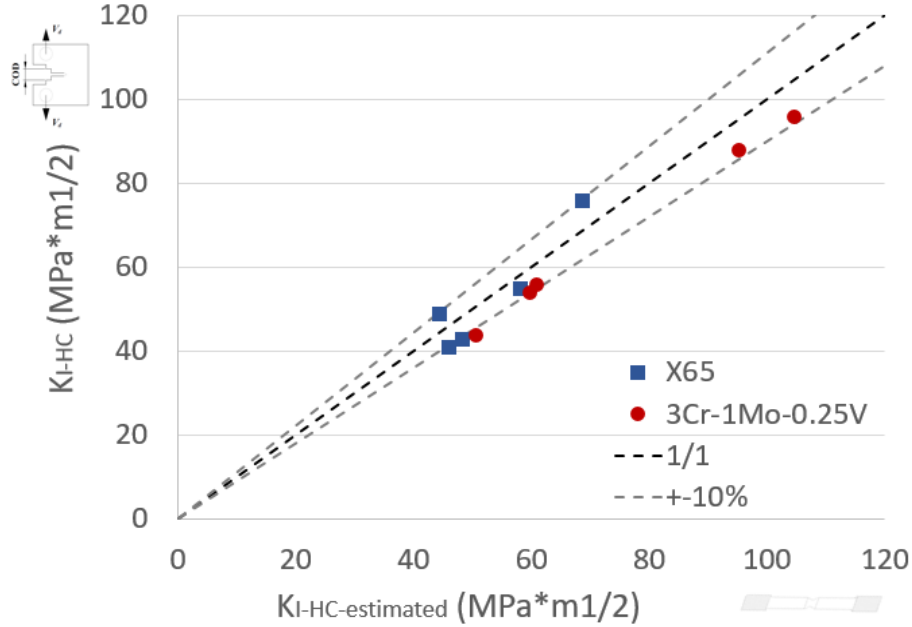


Figure 19. Comparison of K_{I-HC} values obtained from C(T) specimens and from NT 0.5-5 ones.

6.3. Validation analysis by using FAD diagrams

Another way to understand and validate the obtained conclusions is by analysing the obtained results following the structural integrity assessment of the tested geometries using Failure Assessment Diagrams (FAD) [39] [40]. For a given structural component containing a crack, the FAD present a simultaneous assessment of both the fracture and plastic collapse processes given by the normalised parameters K_r and L_r respectively, whose expressions are:

$$K_r = \frac{K_I}{K_{mat}} \quad (6)$$

$$L_r = \frac{P}{P_L} \quad \text{or} \quad L_r = \frac{\sigma_{ref}}{\sigma_Y} \quad (7)$$

K_I being the stress intensity factor, and K_{mat} being the material fracture resistance measured by the stress intensity factor (e.g., K_{IC} , K_{JC} , $K_{J0.2}$, etc), P being the applied load, P_L being the plastic collapse load, and σ_{ref} being the reference stress and σ_Y being the material yield stress. So, the component assessment point is defined through a pair of K_r and L_r coordinates, and the limiting conditions by the Failure Assessment Line (FAL), given in bibliography, as in [39].

For the present case, the FAD diagrams of both materials for NT 0.5-5 geometry, and in them the $(K_r - L_r)$ coordinates for each one of the cases studied, are represented in Figure

20. For its calculation option 1 of BS 7910:2013 [39] for materials that do not have yield plateau (continuous yielding) was used. K_r is calculated using the estimated K_{I-HC} values and L_r using the instability loads, P_{max} , as follows.

$$K_r = \frac{K_{I-HC \text{ estimated}}}{K_{J0.2-air}} \quad (8)$$

$$L_r = \frac{P_{max}}{P_{max-air}} \quad (9)$$

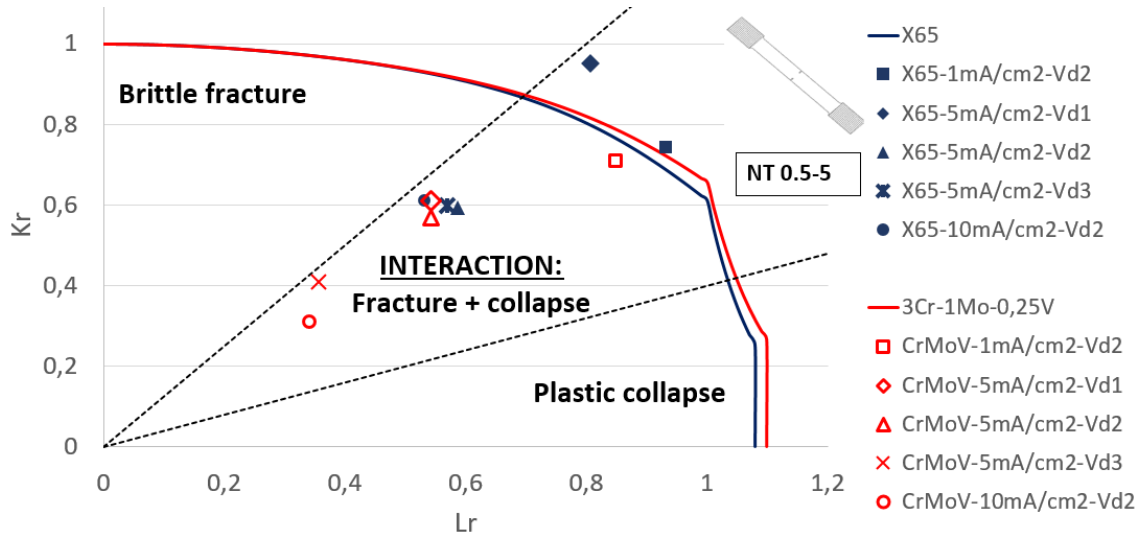



Figure 20. FAD assessment of NT 0.5-5 samples studied.

If the previously presented FAD diagram is qualitatively analysed, firstly it can be appreciated that in all the cases studied the failure mode is an interaction of brittle fracture + plastic collapse, which justifies the use of the FAD as the proper tool to assess these situations [41] [42].

On the other hand, it can be observed that in the less embrittled scenarios the failure $K_r - L_r$ representation is close to the FAL line, while in the more brittle cases the points far away from FAL line, indicating that those specimens failed due to a stronger hydrogen effect and its level.

Finally, for the blunter geometry, NT 5-5, a FAD analysis cannot be carried out because K_{I-HC} cannot be estimated, but the coordinate L_r can be calculated according to expression (7), as presented on Table 10, where it can be observed how in practically all the cases the L_r value is very close to 1, which means that the failure will be caused by plastic collapse, under mechanisms lightly more brittle than those presented in air. Nevertheless, there were two cases in X65 steel, 5 mA/cm² at V_{d3} and 10 mA/cm² at V_{d2}, with L_r values of 0.75 and 0.51 respectively, but in these cases (ie. Figure 12) the failure mode is still caused by a plastic collapse initiated in the central area of the specimen, even if, due to the embrittling environment, the fractographical analysis shows the presence of more brittle features.

Table 10. *L_r values calculate for NT 5-5 tests of both steels.*

| X65 $L_r = P_{\max}/P_y$ NT 5 - 5 | | |  | 3Cr-1Mo-0.25V $L_r = P_{\max}/P_y$ NT 5 - 5 | | |
|---|-----------------------------|------------------------------|---|---|-----------------------------|------------------------------|
| I = 1 mA/cm ² | I = 5 mA/cm ² | I = 10 mA/cm ² | | I = 1 mA/cm ² | I = 5 mA/cm ² | I = 10 mA/cm ² |
| - | 0.88 | - | V _{d-1} (m/s) 0.40·10 ⁻⁷ | - | 1.0 | - |
| 0.89 | 0.86 | 0.51 | V _{d-2} (m/s) 0.68·10 ⁻⁸ | 0.92 | 0.97 | 0.95 |
| - | 0.75 | - | V _{d-3} (m/s) 0.94·10 ⁻⁹ | - | 0.90 | - |

7. Conclusions

The analysis of the obtained results in this paper allowed to clarify qualitatively, as well as quantitatively, the influence of environmental, geometrical and loading rate factors on the hydrogen embrittlement processes, including subcritical crack initiation and propagation mechanisms, as well as mechanical and fracture behavior parameters. For this purpose, equivalent testing rates were defined for C(T), NT 0.5-5 and NT 5-5 geometries, in order to assure analogous local strain rate conditions in the different geometries. The obtained differences in behaviour have been justified through the corresponding hydrostatic stress and equivalent plastic strain states and the hydrogen concentration distribution at a local level.

The differences in the cracking initiation areas and subsequent failure processes in the specimen cross section are associated with hydrostatic stress and its effect on the increase in local hydrogen concentration. Thus, in NT 0.5-5 cracks the initiation is established at the notch tip to produce a final crack, while in NT 5-5 the initiation occurs in the central area, producing a failure due to plastic collapse. Those conclusions are illustrated and summarised in Figure 21, which shows the schematic failure processes for the two geometries tested together with a profile picture of a real test in each case.

The subcritical cracking conditions in NT 0.5-5 reach the instability as a function of the loss of fracture toughness of the material due to hydrogen embrittlement, whose value has been validated by comparison with the values obtained from standard C(T) specimens fracture tests in the same environmental conditions. Also, failure mechanisms have been validated by comparison with those corresponding to the relative situation in failure assessment diagrams (FAD).

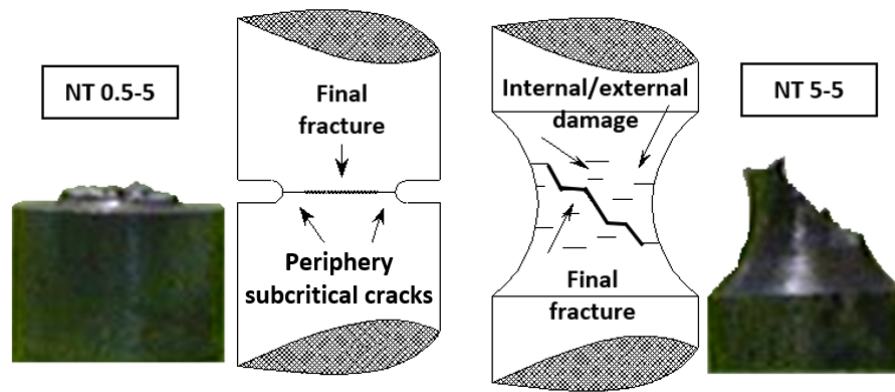


Figure 21. Schematic failure processes and profile view of fracture section for the two geometries studied.

References

- [1] www.fircroft.com/blogs/the-6-biggest-offshore-structures-in-the-world-83272314444, "(Accessed August 2020)".
- [2] J.P. Hirth, "Effects of hydrogen on the properties of iron and steel," *Metallurgical transactions*, vol. 11, no. A, pp. 861-890, 1980.
- [3] A.W. Thomson, I.M. Bernstein, "Hydrogen effects in metals," *Metallurgical Society of AIME*, pp. 291-ss, 1980.
- [4] R.P. Gangloff, "Hydrogen assisted cracking of high strength alloys," *Charlottesville*, 2003.
- [5] A.M. Brass, J. Colet-Lacoste, "Surface phenomena on pure iron during electrochemical permeation tests," *Hydrogen transport & cracking in metals; The institut of materials*, pp. 142-154, 1995.
- [6] F. Gutiérrez-Solana, M. Elices, "High pressure hydrogen behavior of pipeline steels," *Current solutions to hydrogen problems in steels; ASM*, pp. 181-185, 1982.
- [7] R. Gibala, A.J. Kumnick, "Hydrogen trapping in iron and steels," *Hydrogen embrittlement and stress corrosion cracking, ASM*, pp. 61-77, 1984.
- [8] P. Lacombe, M. Aucouturier, J. Chêne, "Hydrogen trapping and hydrogen embrittlement," *Hydrogen embrittlement and stress corrosion cracking, ASM*, pp. 79-102, 1984.
- [9] I.M. Bernstein, A.W. Thomson, "The role of microstructure in hydrogen embrittlement," *Hydrogen embrittlement and stress corrosion cracking, ASM*, pp. 135-152, 1984.
- [10] A. Turnbull, "Modeling of environmental assisted cracking," *Corrosion science*, vol. 34, pp. 921-960, 1993.

- [11] Pressouyre G.M., Blondeau R., Primon G., Cadiou L., "Proceedings of the 1st International Conference on Current Solutions to Hydrogen Problems in Steels," *ASM Metals Park, Ohio, OH, Interrante C.G., and Pressouyre G.M., eds.*, pp. 212-218, 1982.
- [12] Pontremolli M. and Buzzichelli G., "Composition, microstructure and properties of pipeline steels with high H.I.C. and SSCC resistance," *BTF Special Issue*, pp. 59-67, 1988.
- [13] B. Arroyo, J.A. Álvarez, F. Gutiérrez-Solana, A. Cayón, Y.J. Jirón, A.R. Seco, "A Proposal for the Application of Failure Assessment Diagrams to Subcritical Hydrogen Induced Cracking Propagation Processes," *Metals*, vol. 9, no. 670, 2019.
- [14] R. Fernández-Sousa, C. Betegón, E. Martínez-Pañeda, "Analysis of the influence of microstructural traps on hydrogen assisted fatigue," *Acta Materialia*, vol. 199, pp. 253-263, 2020.
- [15] H.P. Van Leeuwen, "The kinetics of hydrogen embrittlement: a quantitative diffusion model," *Engineering Fracture Mechanics*, vol. 6, pp. 141-164, 1974.
- [16] M.A. Astiz, "Hydrogen diffusion analysis in metals," *Computational Methods for Non-linear Problems*; Ed. C. Taylor, D.R. Owen & E. Hinton, Pineridge Press, 1987.
- [17] P. Sofronis, R.M. McMeeking, "Numerical analysis of hydrogen transport near blunting crack tip," *Journal of the Mechanics and Physics of Solids*, vol. 37, no. 3, pp. 317-350, 1989.
- [18] A.H.M. Krom, R.W.J. Koers, A. Bakker, "Hydrogen transportation near blunting crack tip," *Journal of the Mechanics and Physics of Solids*, vol. 47, pp. 971-992, 1999.
- [19] E. Martínez-Pañeda, A. Díaz, L. Wright, A. Turnbull, "Generalised boundary conditions for hydrogen transport at crack tips," *Corrosion Science*, vol. 173, no. 108698, 2020.
- [20] González J.J., Gutiérrez-Solana F., Varona J.M., "The effects of microstructure, strength level, and crack propagation mode on stress corrosion cracking behavior of 4135 steel," *Metallurgical and Materials Transactions A*, vol. 27A, pp. 281-290, 1996.
- [21] M.A. Astiz J.A. Álvarez F. Gutiérrez-Solana, "Modelo numérico para analizar el efecto del hidrógeno sobre los procesos de fisuración dúctil," *Anales de mecánica de la fractura (Spanish Group of Fracture)*, vol. 15, no. (<http://www.gef.es/PDF/15/Anales15-010.pdf>), pp. 79-84, 1998.
- [22] Gutiérrez-Solana F., Valiente A., González J.J., Varona J.M., "A strain-based fracture model for stress corrosion cracking of low-alloy steels," *Metallurgical and Materials Transactions A*, vol. 27A, pp. 291-304, 1996.
- [23] J.A. Álvarez, F. Gutiérrez-Solana, "An Elastic-Plastic Fracture Mechanics Based Methodology to Characterize Cracking Behaviour and its Applications to Environmental Assisted Processes," *Nuclear Engineering and Design*, vol. 188, pp. 185-202, 1998.
- [24] Specification API 5LD, Specification for CRA clad or lined steel pipe, American Petroleum Institute, 2009.

- [25] CEN - European Committee for Standardization, "Standard EN 10028-2," *Flat products made of steels for pressure purposes - Part 2: Non-alloy and alloy steels with specified elevated temperature properties*, 2003.
- [26] UNE-EN ISO 6892-1, "Metallic materials - Tensile testing - Part 1: Method of test at room temperature (ISO 6892-1:2019)," 2020.
- [27] ASTM E8 / E8M 16a, "Standard Test Methods for Tension Testing of Metallic Materials," 2016.
- [28] ESIS Standard ESIS P2-92, "ESIS Procedure for Determining the Fracture Behaviour of Materials," *European Structural Integrity Society*, 1992.
- [29] ASTM E1820-20a, "Standard Test Method for Measurement of Fracture Toughness".
- [30] ASTM E384 - 17, "Standard Test Method for Microindentation Hardness of Materials".
- [31] Pressouyre G.M., Bernstein I.M., "An Example of the Effect of Hydrogen Trapping on Hydrogen Embrittlement," *Metallurgical Transactions*, vol. 12, no. A, pp. 835-844, 1981.
- [32] ISO 7539, Parts 1 to 9, Corrosion of Metals and Alloys, 2011.
- [33] B. Arroyo, L. Andrea, J.A. Álvarez, S. Cicero, R. Lacalle, "Analysis of samples cleaning methods prior to hydrogen content determination in steel," *Metals*, Vols. 10, Issue 6, no. 723, 2020.
- [34] V. Kumar, M. German, C.F. Shih, "An Engineering Approach to Elastic-Plastic Solid," *Research project EPRI-1931; General Electric Company, Schenectady, NY, USA*, 1981.
- [35] ESIS P6-98, "Procedure to measure and calculate material parameters for the local approach to fracture using notched tensile specimens," *TC8 Committee on Numerical Methods, European Structural Integrity Society*, March 1998.
- [36] L. Lesne et. Al., "Application of New Fracture Mechanics Concepts to Hydrogen Damage Evolution," *Final Report. European Commission, Technical Steel Research*, no. Contract No 7210-PR/110, 2003.
- [37] F. Gutiérrez-Solana Salcedo, J.M. Alegre Calderón, J. Pérez Gil, J.A. Álvarez Laso, I. Carrascal Vaquero, J.A. Polanco Madrazo, "Sistema de medida de la variación perimetral en ensayos de materiales," *Spanish invention patent, OFICINA ESPAÑOLA DE PATENTES Y MARCAS*, 1999 (presented) 2003 (published).
- [38] I.M. Bernstein, G.M. Pressouyre, "Role of traps in the microstructural control of hydrogen embrittlement of steels," *Noyes Publ, Park Ridge, NJ, Pittsburgh*, 1988.
- [39] BS7910:2013, "Guide to methods for assessing the acceptability of flaws in metallic structures," *London: British Standards*, 2013.
- [40] FITNET Fitness-for-Service (FFS) Procedure, " Volume 1," *Kocak M, Webster S, Janosch JJ, Ainsworth RA, Koers R, editors. Geesthacht: GKSS Forschungszentrum*, 2008.

- [41] Gutiérrez-Solana F., Ruiz-Ocejo J., Bannister A.C., Ainsworth R.A., Kim Y-J., "Developement of the SINTAP failure assesment diagrams for compatibility with crack driving force approaches," *paper OMAE99-2042, Newfoundland, Canada*, 1999.
- [42] Ruiz-Ocejo J., Gutiérrez-Solana F., "Recomendaciones para el refinamiento de variables en el procedimiento SINTAP de evaluación de la integridad estructural de componentes fisurados," *Anales de mecánica de la fractura (Grupo Español de Fractura)*, vol. 16, pp. 482-487, 1999.
- [43] T.E. García, C. Rodríguez, F.J. Belzunce, I. Peñuelas, B. Arroyo, "Developement of a methodology to study the hydrogen embrittlement of steels by means of the Small Punch test," *Material science & engineering A*, vol. 626, pp. 342-351, 2015.
- [44] B. Arroyo, J.A. Álvarez, R. Lacalle, C. Uribe, T.E. García, C. Rodríguez, "Analysis of Key Factors of Hydrogen Environmental Assisted," *Materials Science and Engineering A*, vol. 691, pp. 180-194, 2017.